GeoScienceWorld
Lithosphere
Volume 2022, Article ID 6387274, 23 pages
https://doi.org/10.2113/2022/6387274

Lithosphere

*Research Article*

# Earthquake-Induced Stress Amplification and Rock Fragmentation within a Deep-Seated Bedding Fault: Case Study of the Daguangbao Landslide Triggered by the 2008 Wenchuan Earthquake (Ms = 8.0)

**Shenghua Cui, Xiangjun Pei, Hailong Yang, Qingwen Yang, and Ling Zhu**

*State Key Laboratory of Geohazard Prevention and Geoenvironment Protection, Chengdu University of Technology, Chengdu 610059, China*

Correspondence should be addressed to Xiangjun Pei; peixj0119@tom.com and Hailong Yang; yhl826325@126.com

Received 17 December 2021; Accepted 12 August 2022; Published 5 September 2022

Academic Editor: Shuo Zhang



The 2008 Wenchuan Ms 8.0 earthquake triggered the Daguangbao (DGB) landslide, of which the shear surface belongs to a thrust bedding fault 400 m below the carbonate slope. After the landslide, a 1.8 km-long inclined sliding face (0.3 $km^2$) was exposed in the south source area. By using shaking table test, the contributions of the fault to the landslide sliding have been studied in this paper. The bedding fault in the test model is simplified as a weak layer with small elasticity and the carbonate layers as a hard layer with high elastic modulus, which is 296 times the weak one. The test records larger displacement amplitude in the upper hard layer than that in the lower one and larger pressure amplitude in the weak layer than that in the hard ones. We ascribed the stress amplification in the weak layer to time delay of shaking wave as wave velocity in the weak layer is only 1/15 of that in the hard layers. Such time delay gives rise to phase differences between the hard layers during shaking. The compressive stress amplification occurs in the weak layer when the upper hard layer moves downwards relative to the lower one; otherwise, tensile stress amplification occurs. It is suggested that this kind of stress amplification triggered an extensive fragmentation of the bedding fault rock mass during the Wenchuan earthquake, which can be verified by a good deal of gentle-dip and steep-dip cracks observed on site. It is proposed that stress amplification had caused a fast dropping of shear strength in the bedding fault to enhance the suddenness of DGB landslide initiation.

## 1. Introduction

Weak layer is thin stratum with weak mechanical properties in slope but widely develops in active orogenic belts. The common types of weak layer include weathered crust, soft rock layer, and bedding fault. Time-dependent deformation occurs in the weak layer. If friction angle is smaller than strata inclination, shear failure of slope along the weak layer will occur. Therefore, the weak layer is usually reported as the key determinant to slope stability [1–4]. The gravity deformation process of the weak layer is relatively slow but will be promoted subjected to earthquake and rainfall.

Wenchuan earthquake and other strong earthquakes that occurred on Tibet Plateau have triggered a mass of landslides [5–11]. Previous studies on such earthquake-caused landslides show that stratiform rock stratum area is usually featured by concentrated large-scale landslides because of the existence of weak interlayer [12, 13]. The weak layer deformation and failure during earthquake are a part of the key content of understanding such landslide causes. Due to the isolation effect of the weak layer on seismic energy [14], the existence of the weak layer will weaken the acceleration response of rock slopes [15]. Shaking table test results have suggested that the isolation effect is related to the thickness of the weak interlayer [16]. The amplification of peak acceleration was observed at the crest of model slope with thinner weak layer; otherwise, it was observed at below the crest of model slope

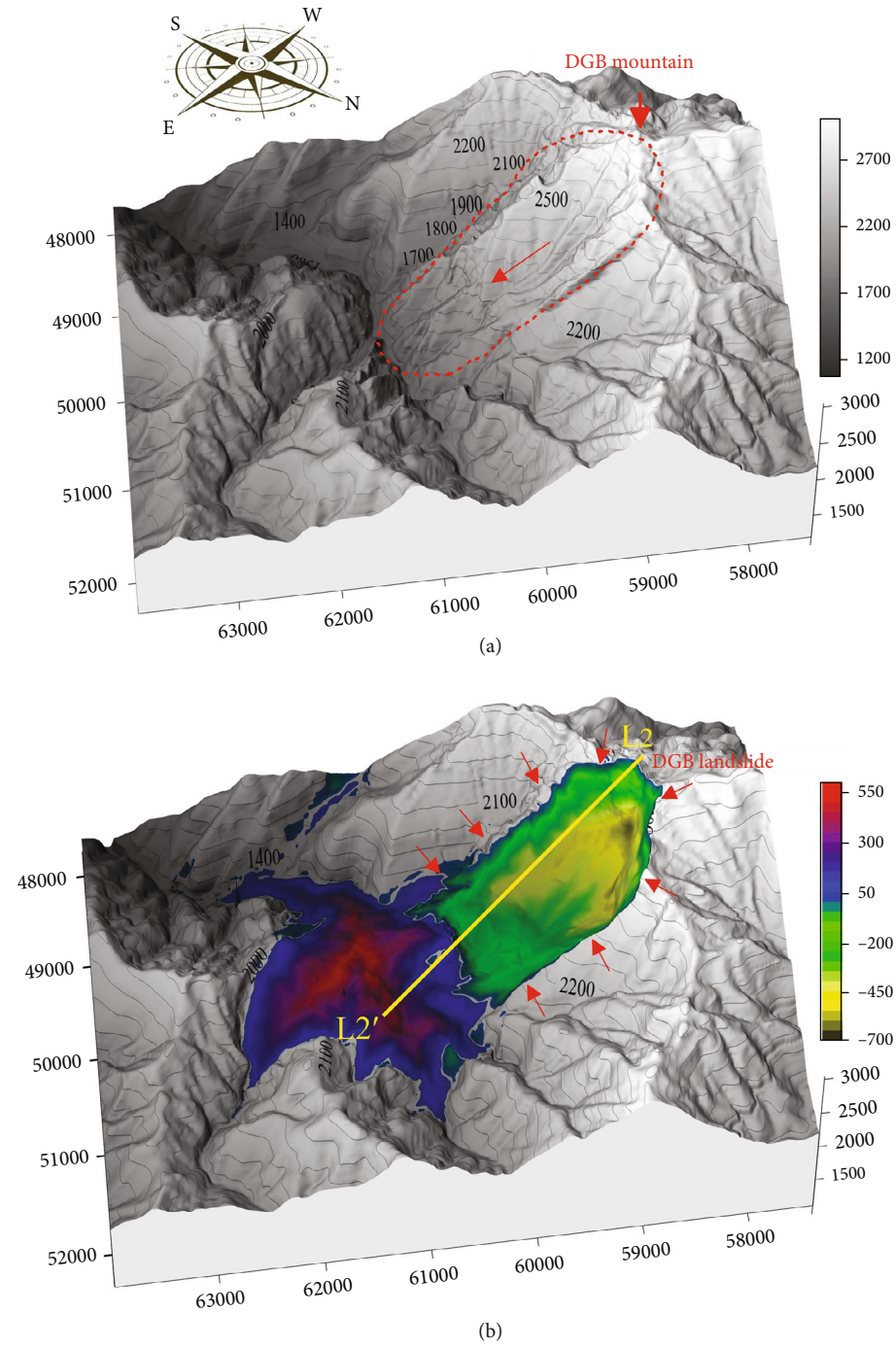


Figure 1: 3D mode of the DGB landslide. (a) Before landslide and (b) after the landslide (section lines L2-L2′).

(thick weak layer) [17]. When the seismic wave passes through the weak interlayer, the seismic energy is redistributed in the upper part of rock slopes [18], which will inevitably affect the stability and failure mode of the slope [16].

The DGB landslide located in Anzhou District, Sichuan Province, is the largest landslide triggered by the 2008 Wenchuan Earthquake. The landslide is 85 km away from the epicenter and 4 km away from the surface rupture. Remote sensing images of the landslide site (e.g., [19, 20]) provide detailed information about the geometry and landform before the landslide. The landslide caused a 400 m-deep failure (Figure 1(a)). The sliding mass formed a 600 m-thick landslide dam (Figure 1(b)) in the valley of 640 m high. The numerical simulation method such as discontinuity deformation analysis (DDA) has been carried out to simulate the initiation, movement, and deposit of DGB landslide [21, 22]. Although the DGB landslide has

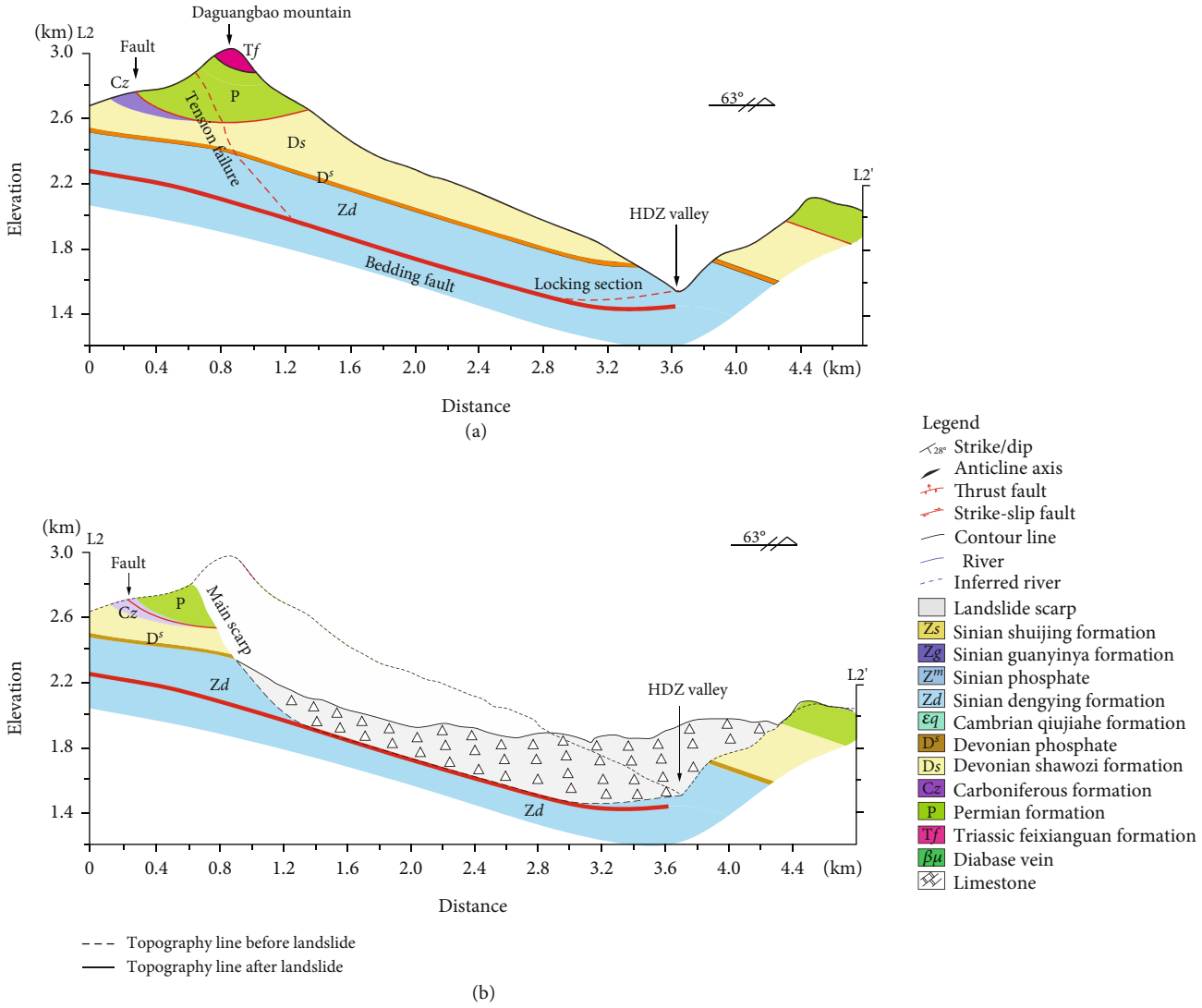


Figure 2: Section map of the DGB landslide. (a) Before landslide and (b) after the landslide.

been attached with great attention since it happened, researchers still have different views on its cause. For example, based on numerical simulation results, it was confirmed that vertical seismic forces have a significant impact on the initiation of coseismic landslide [23, 24]. Zhang et al. [21] and Pei et al. [25] carried out detailed site investigations on the landslide slip surface, and it is considered that the joints and local faults developed in DGB slope are favorable for the occurrence of DGB landslide.

The DGB landslide was a wedge failure [26], the earthquake must be the direct inducement to it [27], and the prerequisite was gravity deformation [10]. A 730 m long scarp, 1.5 km long release surface and 1.8 km long sliding face were, respectively, found to the west, north, and south of the landslide. Based on Cui et al. [28], the shear failure of sliding face had a significant contribution to triggering the landslide. The friction characteristics of the sliding surface have a significant impact on the initiation and long-distance movement of DGB landslide during the earthquake [28]. Recently, after digging a tunnel (2 m in length) at the foot of the southern scarp of the landslide, the sliding zone of the landslide was found to be generated in a preexisting bedding fault [28]. The damage of the fault during the earthquake has become one of the researches focused on the DGB landslide. During the earthquake, the rock along the fault might incur intense seismic-related deformation. The rapid failure of the landslide can be associated with the weak of the rock mass strength of the bedding fault both before and during the 2008 Wenchuan earthquake.

Therefore, taking DGB landslide as the prototype, model slope with a horizontal weak interlayer, was designed to conduct shaking table model tests. The embedded sensors were used to obtain the dynamic response data inside the model. By comparing the response difference between the weak

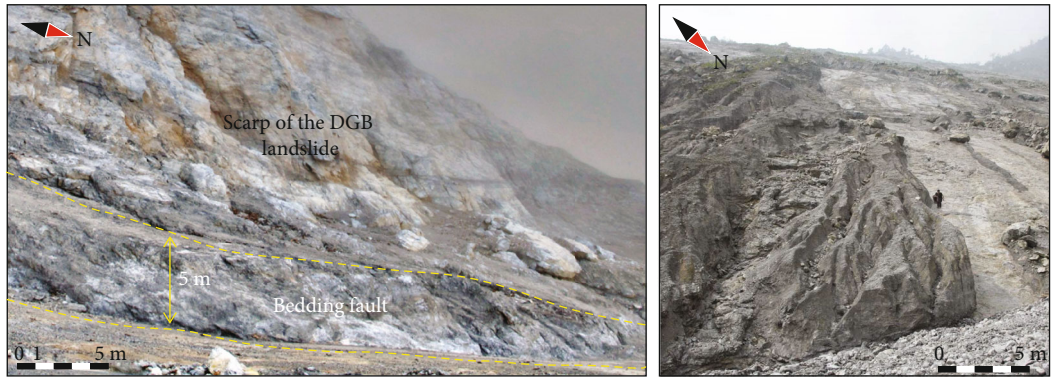


Figure 3: Photo showing the bedding fault (a) observed at the foot of the landslide scarp and (b) observed on the landslide sliding area.

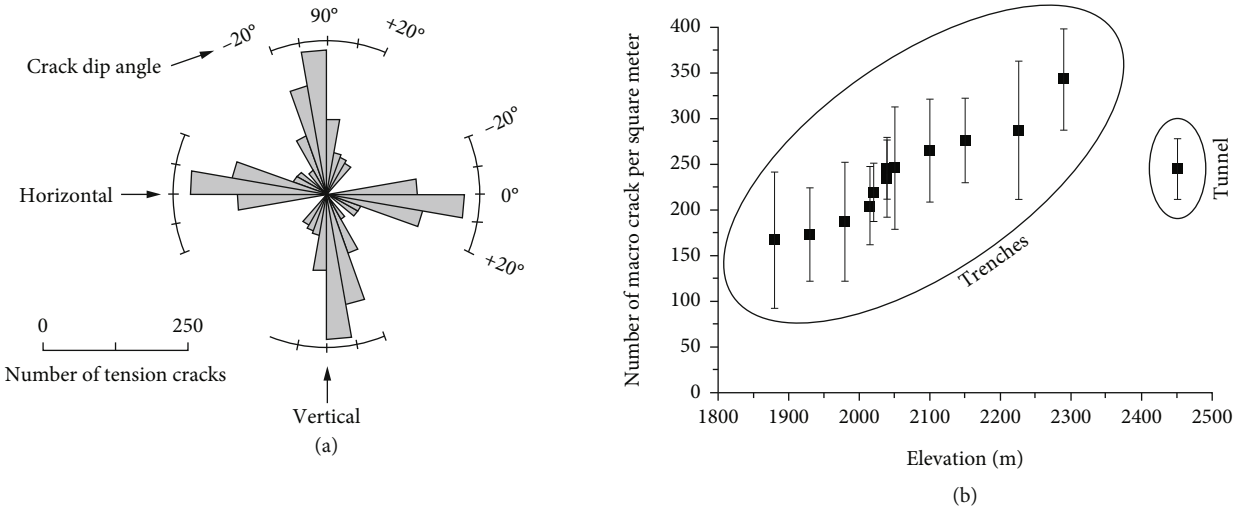


Figure 4: Cracks investigated in the trenches and tunnel dug in the bedding fault. (a) Crack dip angle data and (b) number per square meter.

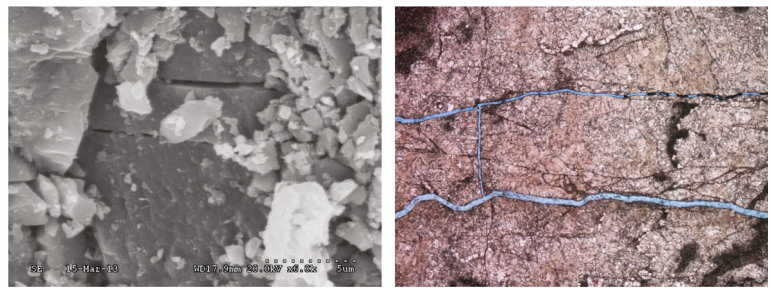


Figure 5: Microcrack investigations of the bedding fault rock mass. (a) SEM image showing transgranular microcracks and (b) rock slice image showing perpendicular microcracks.

interlayer and hard layer, the possible stress conditions caused seismic deformation of fault are analyzed, and the contribution of the dynamic failure of the weak interlayer during the earthquake to the initiation of seismic landslide is revealed.

## 2. Daguangbao Landslide

*2.1. Previous Study.* Huang et al. [29] first report that the Ms 8.0 Wenchuan earthquake of 2008 has triggered a large-scale landslide in the Paleozoic strata in northwestern

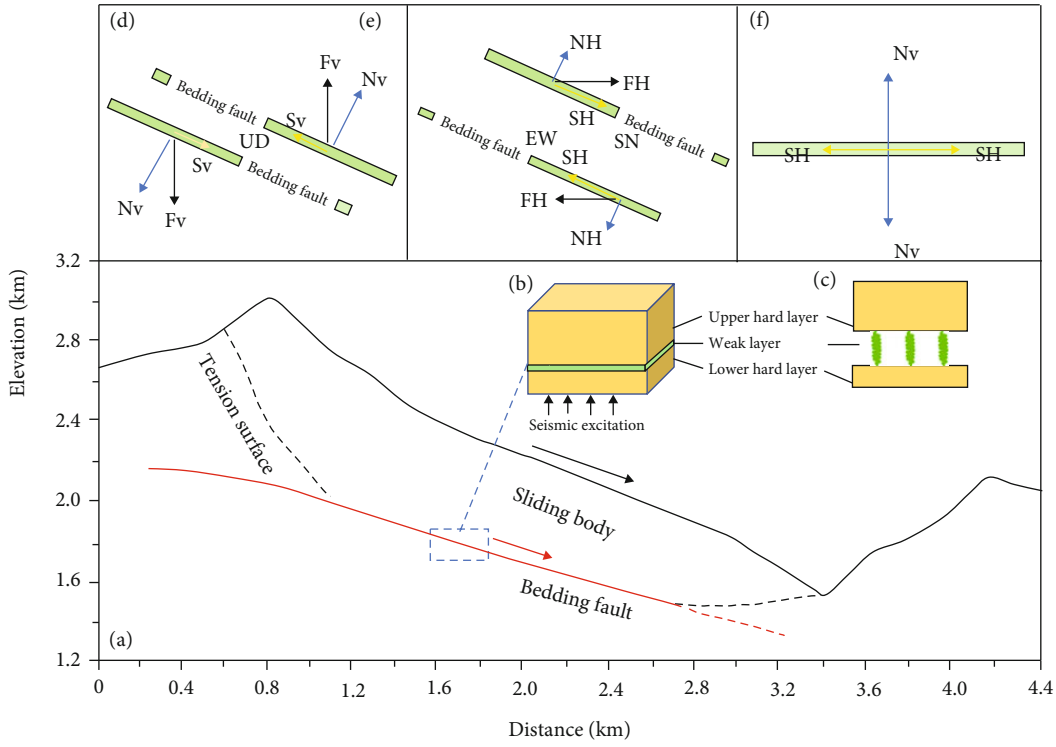


FIGURE 6: (a) Geological model of the DGB landslide, (b) block model used in our test, and (c) spring model used for deformation analysis by assuming the fault zone as elastic layer. (d) Vertical and (e) horizontal stress decompositions of the bedding fault in the geological model. (f) Stress composition of the weak layer in the block model. Fv and Fh are the vertical and horizontal seismic forces, respectively. Nv and SH are the seismic forces perpendicular and parallel to the bedding fault, respectively.

TABLE 1: Similarity system for shaking table test.

| No. | Parameters | Dimension MLT | Dimensionless $\pi$ terms | Similarity relationship | |
|---|---|---|---|---|---|
| | | | | Rock mass | Weak interlayer |
| 1 | Density, $\rho$ | $[M][L]^{-3}$ | Control variable | $C_\rho = 1$ | $C_\rho = 1$ |
| 2 | Elastic modulus, $E$ | $[M][L]^{-1}[T]^{-2}$ | Control variable | $C_E = 200$ | $C_E = 100$ |
| 3 | Time, $t$ | [T] | Control variable | $C_t = 10$ | $C_t = 10$ |
| 4 | Geometrical size, $l$ | [L] | $\pi_l = l/(\rho^{-0.5}E^{0.5}t)$ | $C_l = C_\rho{}^{-0.5}C_E{}^{0.5}C_t = 141$ | $C_l = C_\rho{}^{-0.5}C_E{}^{0.5}C_t = 100$ |
| 5 | Poisson's ratio, $\mu$ | [1] | $\pi_\mu = 1$ | $C_\mu = 1$ | $C_\mu = 1$ |
| 6 | Cohesion, $c$ | $[M][L]^{-1}[T]^{-2}$ | $\pi_c = c/E$ | $C_c = C_E = 200$ | $C_c = C_E = 100$ |
| 7 | Internal friction angle, $\varphi$ | [1] | $\pi_\varphi = 1$ | $C_\varphi = 1$ | $C_\varphi = 1$ |
| 8 | Stress, $\sigma$ | $[M][L]^{-1}[T]^{-2}$ | $\pi_\sigma = \sigma/E$ | $C_\sigma = C_E C_\varepsilon = 200$ | $C_\sigma = C_E C_\varepsilon = 100$ |
| 9 | Strain, $\varepsilon$ | [1] | $\pi_\varepsilon = 1$ | $C_\varepsilon = 1$ | $C_\varepsilon = 1$ |
| 10 | Frequency, $f$ | $[T]^{-1}$ | $\pi_\omega = f/t^{-1}$ | $C_f = C_t{}^{-1} = 0.1$ | $C_f = C_t{}^{-1} = 0.1$ |
| 11 | Displacement, $u$ | [L] | $\pi_u = u/(\rho^{-0.5}E^{0.5}t)$ | $C_u = C_\rho{}^{-0.5}C_E{}^{0.5}C_t = 141$ | $C_u = C_\rho{}^{-0.5}C_E{}^{0.5}C_t = 100$ |
| 12 | Velocity, $v$ | $[L][T]^{-1}$ | $\pi_v = v/(\rho^{-0.5}E^{0.5})$ | $C_v = C_\rho{}^{-0.5}C_E{}^{0.5} = 14$ | $C_v = C_\rho{}^{-0.5}C_E{}^{0.5} = 10$ |
| 13 | Acceleration, $a$ | $[L][T]^{-2}$ | $\pi_a = a/(\rho^{-0.5}E^{0.5}t^{-1})$ | $C_a = C\rho^{-0.5}C_E{}^{0.5}C_t{}^{-1} = 1.4$ | $C_a = C_\rho{}^{-0.5}C_E{}^{0.5}C_t{}^{-1} = 1$ |

Sichuan Province. With the volume estimated at 1.1–1.2 $km^3$ [29–32], the landslide is defined as the largest landslide triggered by Wenchuan earthquake [32].

The sliding surface of the DGB landslide is in dolomite layer, and its dip angle along the sliding direction is only 16° (Figure 2). According to the section map, the sliding

Table 2: Physical and mechanical parameters for prototype and test model.

| Lithology | Density $\rho$/g.cm$^{-3}$ | Poisson ratio $\mu$ | Elastic modulus E/MPa | Friction angle $\varphi$ (°) | Cohesive forces $c$ (kPa) | Compression strength $\sigma_c$ (MPa) |
|---|---|---|---|---|---|---|
| Prototype | | | | | | |
| Hard rock | 2.7 | 0.17 | 60000 | 42 | 14160 | 200 |
| Weak interlayer | 2.3 | 0.36 | 94 | 25 | 1050 | 33 |
| Model | | | | | | |
| Hard rock | 2.6 | 0.17 | 278.5 | 42 | 35.4 | 2.1 |
| Weak interlayer | 1.7 | 0.36 | 0.94 | 42 | 9.8 | 0.33 |

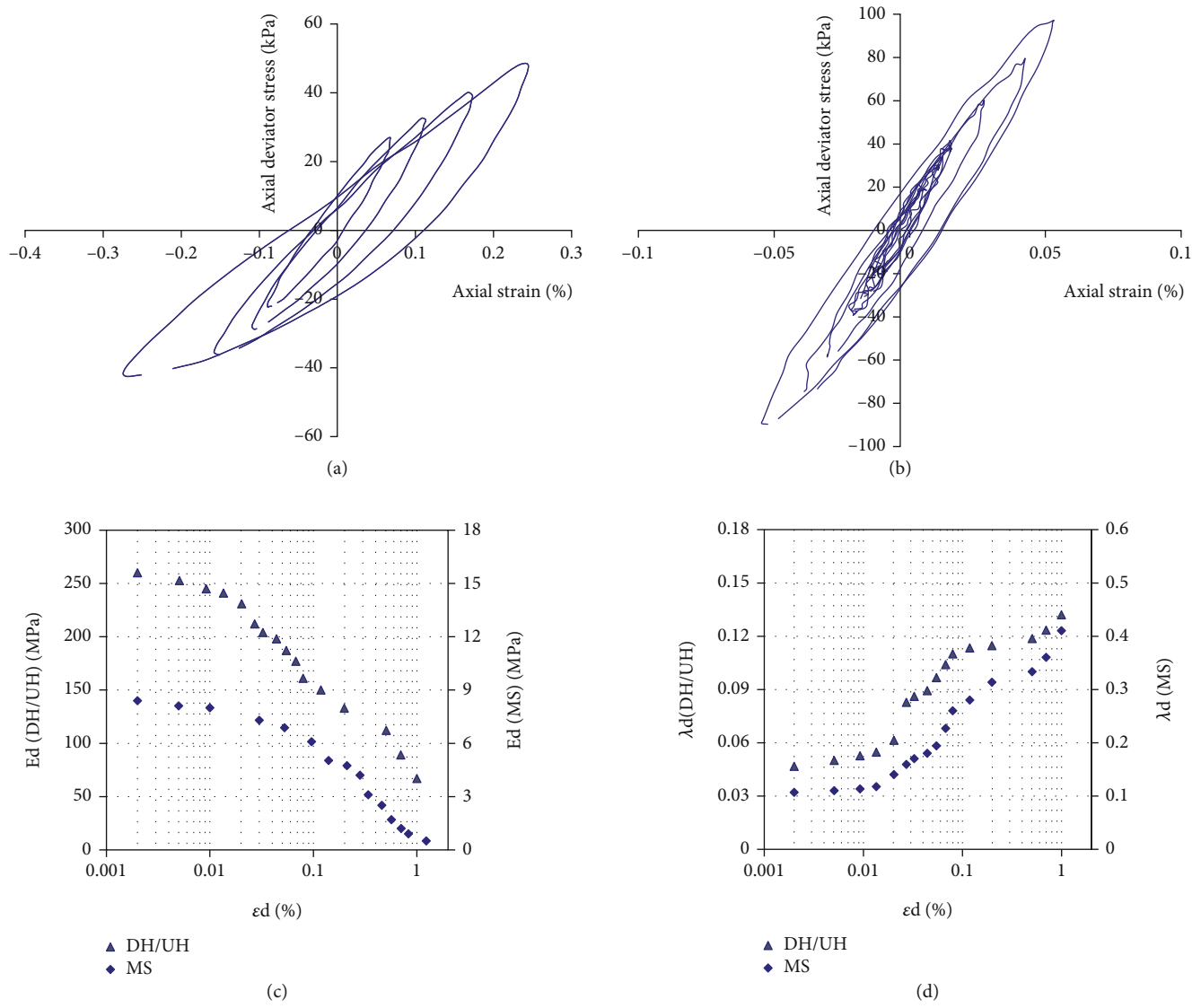


Figure 7: Dynamic properties of the similarity materials used in our shaking table tests. Stress-strain curves of the materials for (a) layer MS and (b) layers UH and DH. Strain-elastic modulus curves of materials for (c) layer MS and (d) layers UH and DH.

surfaces of the DGB landslide stretch under the river bed (Figure 2(a)), which means that the sliding cuts through over a hundred-meter-long carbonate stratum (locking section). When the earthquake happened, there were five people standing right no more than 1 km away from the landslide. According to the interview records of Huang et al. [32], all of the five people saw that the DGB landslide created plenty of soot, which obscured the sight of their surroundings. They heard a loud sound about 60 s later. Huang et al. [32] inferred that this loud sound might be the launching signal

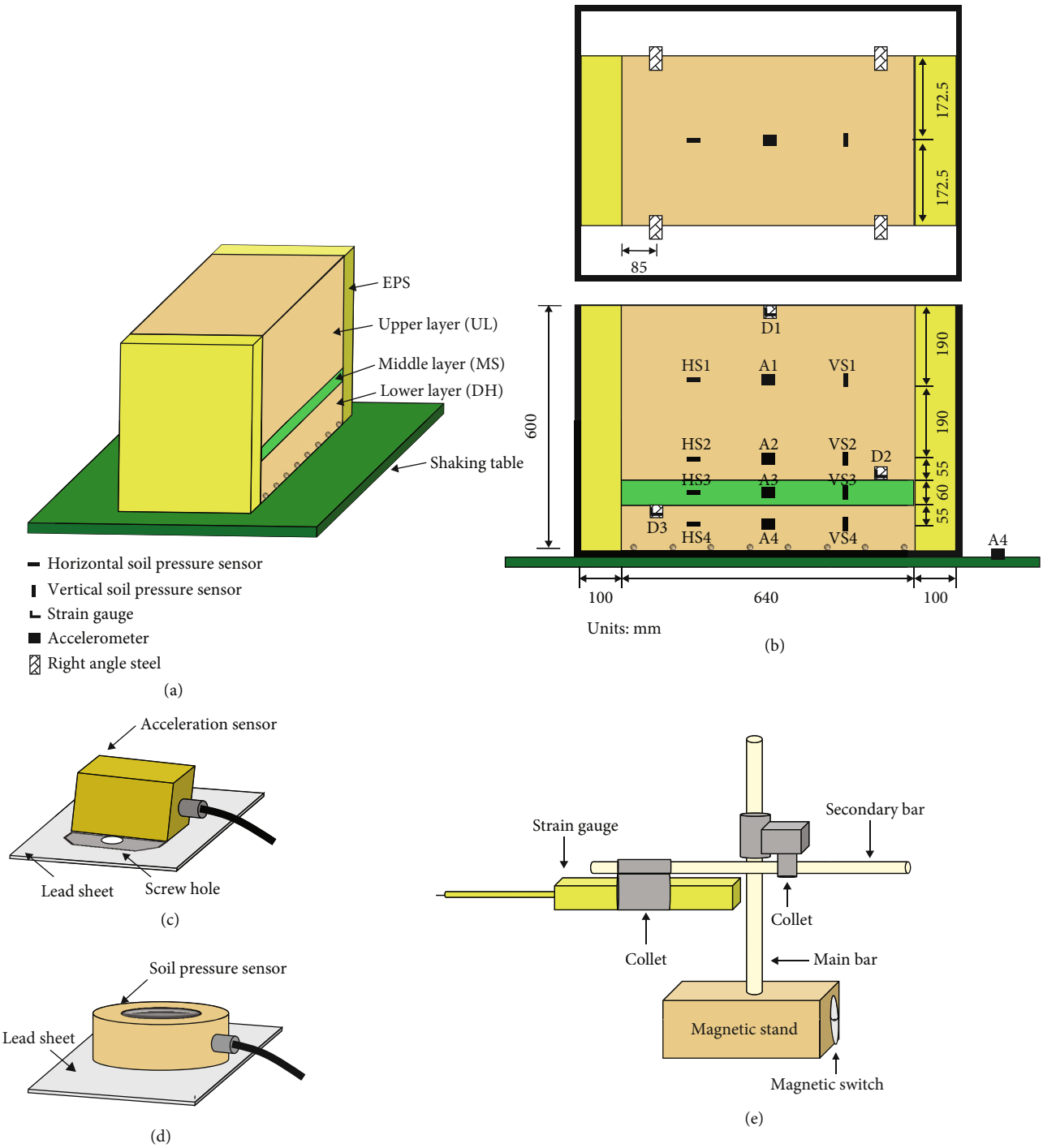


FIGURE 8: Table shaking test model and sensor placement: (a) 3D diagram, (b) vertical and front views, (c) soil pressure sensor, (d) acceleration sensor, and (e) manipulator for deformation sensor.

of the DGB landslide initiation resulting from the breaking of the locking section. Why did the hundred-meter-long locking section fail sharply during the earthquake is still unclear.

Some researchers propose that the landslide was caused by strong horizontal seismic force [33], but the conclusion that "seismic force causes failure" is just an inference for lack of substantial on-site observation and test. Recently, researchers have started to take that the launching of the DGB landslide is related to frictional resistance on the large sliding face or the sudden decline of effective stress. Based on a tunnel under the scarp on rear edge of landslide, it has been determined in Huang et al. [34] that the shear face of landslide belongs to the thrust bedding fault 400 m below

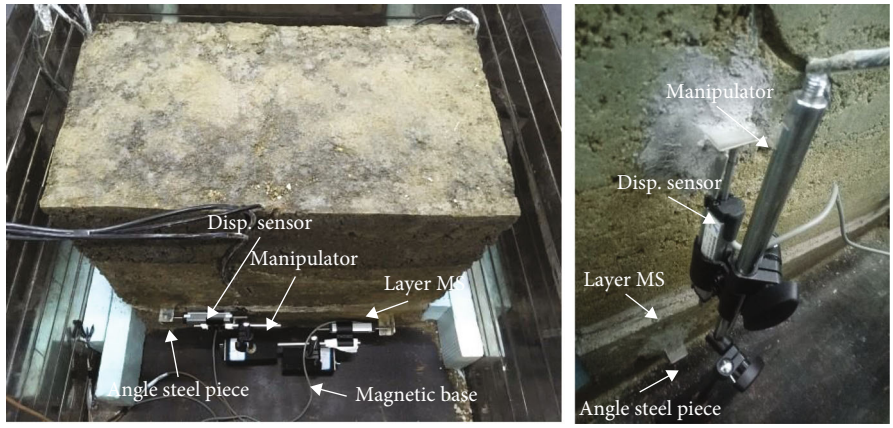


Figure 9: (a) Horizontal and (b) vertical deformation measurements.

the slope. The maximum thickness of the bedding fault is up to 5 m (Figure 3(a)). According to Cui et al. [28], the fault is divided into five parts from bottom to top, which are (1) 2–5 cm-thick yellow mud layer; (2) 10–20 cm-thick mylonite layer mainly made of 0.075–2 cm sized sand grains and 39–71% of particles smaller than 0.1 cm; (3) 1–3 m-thick breccia layer mainly made of breccia particles in the size of smaller than 2 cm, 15–73% of breccia particles of larger than 10 cm, (4) about 2 m thick fragmented rock layer with joint space larger than 20 cm; and (5) more than 10 m thick Sinian system dolomite bedrock with joint space larger than 1 m. On the backside of the slope, outcrops of the bedding fault at three places have been found by Cui [27]. The fault cannot be seen on the 1 : 50000 geologic map [35]. The founding makes the speculation that the fault is distributed continuously within the scope of landslide. After the landslide, some fault materials remained on the sliding surface (Figure 3(b)). The boundary between the fault materials and the bedrock can be easily found.

A layer of 14–24 mm thick loose powdery material is found on the sliding face of the DGB landslide. The powdery material contains 4–12% breccia and 37–83% of particles smaller than 0.1 mm. Slickensides can be observed on the breccia. A tunnel was dug in the fault. The material under powdery is the same as that in the tunnel, but the difference is that there is no powdery material found in the tunnel. Cui et al. [28] proposed that the powdery material layer resulted from the landslide movement and puts forward that shear failure of landslide took place within the fault breccia layer. They gave the failure mode of the DGB landslide and terrain generation model as follows: (1) Wenchuan earthquake gave rise to ground shaking, putting the ridge of the DGB slope under horizontal seismic force. (2) Under the effect of horizontal seismic force, the slope was broken. The sharp decline in the effective stress of basal layer made stress concentrate in the locking section. (3) Shear displacement occurred under the restriction of the bedding fault. The sliding block hits the slope on the other side of river. (4) Landslide went on moving because of inertia and up to the slope on the other side of valley until 500 m high. According to Cui et al. [28], the rock mass fragmentation on the base leads to a sharp decline in shear strength, which is the inducement to the landslide, but the conclusion that earthquake caused fault breakage is still speculation.

Zhang et al. [21] and Wu et al. [36] found through numerical simulation that the horizontal seismic amplification of the DGB slope was greater than its vertical seismic amplification. The DGB landslide mechanism related to horizontal seismic force was also discussed. According to Zhang et al. [23], the DGB slope has vertical seismic amplification, but the amplification mechanism is not clear. And the bedding fault is not taken into consideration in any numerical simulation for the DGB landslide due to the lack of test data of shaking behavior for the fault.

*2.2. Our Observation.* Massive seismic fissures are found within the fault. Some cracks pass through breccia and some extend along the contact face of breccia. For the restriction of particle size or the contact face length, the fissures are short in length but large in number. 85% fresh fissures are gentle-dip ($0° \pm 20°$) and steep-dip ($90° \pm 20°$) fissures (Figure 4(a)). With the sliding face elevation rising from 2000 m to 2200 m, the developing density of fissures increases from 130 to 260 per $m^2$ (Figure 4(b)). Pits and transcrystalline cracks formed by hit are observed by scanning electron microscope (SEM) (Figure 5(a)). And it is found through thin rock slices that these fissures develop horizontally and vertically (Figure 5(b)). The evidence for proving that fissures have to be produced before the landslide initiation is as follows. (1) Fresh fissures are found in the tunnel located at rear rim of the landslide. This area is not affected by the landslide, which means that these fissures are made by neither unloading nor vibration during sliding. (2) If the fresh fissures are made by unloading of landslide, the density of developed fissures must decrease with the rising of elevation, as the lower the elevation, the thicker the strata on the sliding face, and the greater the unloading, but the density of the fresh fissures increases with the rising of elevation according to the investigation (Figure 4(b)).

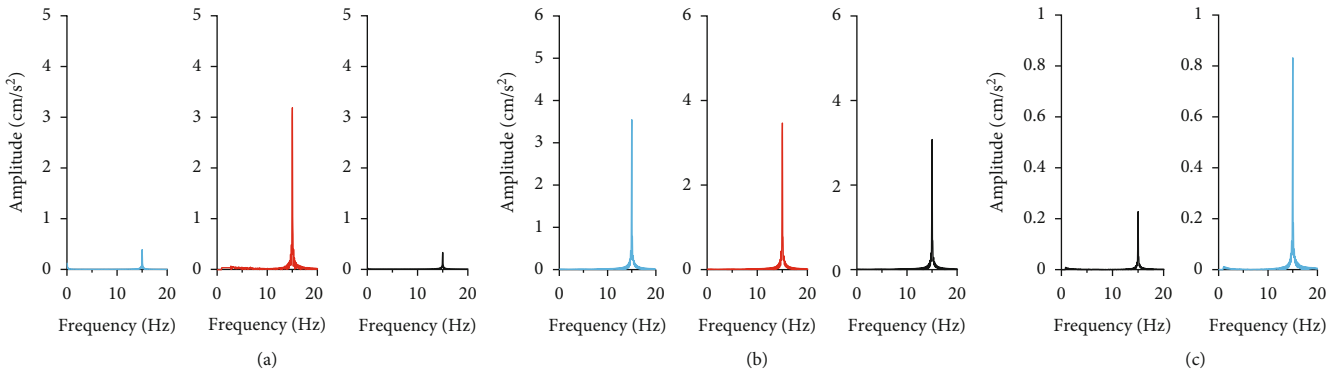


Figure 10: Fourier spectrum of (a) soil pressure, (b) acceleration, and (c) displacement waves.

Shaking table tests were conducted in this study to investigate the cause of the fissures generated during the earthquake.

## 3. Shaking Table Test

*3.1. Test Model.* In this study, the shaking table model test (Figure 6(a)) has been conducted based on the prototype of the DGB landslide which the landslide body was simplified as dolomite rock mass (Figure 6(b)). We tested the elasticity modulus of fault and dolomite under uniaxial cyclic loading, and the fault's elasticity modulus is 94 MPa, which is only 1/600 of the dolomites. According to the records on the Wenchuan earthquake around the DGB landslide, the main frequency of the seismic wave is 1–5 Hz, and the wavelength is 1–5 km. The DGB landslide body is 400 m thick, less than half of the seismic wavelength. Thus, we took the dolomite strata as a rigid body and the bedding fault as a linear elastomer (Figure 6(c)). Turn the cataclinal fault horizontal and take the vertical seismic force into consideration (Figures 6(d)–6(f)). Under the effect of vertical seismic force, fault stress is taken as a plane strain problem, and the unit is free from the boundary constraints.

*3.2. Similarity Laws.* Represent the $i$ -$^{th}$ physical quantity in the prototype system ($P$) with $x_i$, corresponding physical quantity in the test system ($M$) with $x_i'$, and define the similarity coefficient ($c_i$) as the ratio of the two physical quantities ($c_i = x_i/x_i'$). After similarity coefficient is confirmed, all physical quantities of the model can be calculated. The purpose of this study is not to reproduce the landslide; so, the elasticity modulus is more important than geometric dimension to distinguish the fault materials from dolomite materials. The elasticity modulus needs to be as accurate as possible. The EPT dimensional system including the basic dimensions of elasticity modulus $E$, density $\rho$, and time $t$ (Table 1) is taken for this paper.

Layers of the model are marked by UH, DH, and MS, respectively. When the scale factor of elasticity modulus of layer MS is 100, the elasticity modulus of layer MS is 0.94 MPa. Layer MS shows good elastic deformation under the elasticity modulus based on the early test results. The elasticity moduli of layers UH and DH under the similarity coefficient 100 are 600 MPa. As the elasticity moduli of available materials are difficult to reach 600 MPa on the premise that sensor works properly and effective data are monitored, the similarity coefficient of elasticity moduli of UH and DH is 200. If the similarity coefficient of fault materials is 200,

Table 3: Test sequence.

| No. | Characteristics and type of the input waveform |
|---|---|
| Case 1 | WN-1; intensity: 0.05 g |
| Cases 2-4 | Sine wave, intensity: 0.05 g, frequency: 5, 10, and 15 Hz, respectively |
| Case 5 | WN-2; intensity: 0.05 g |
| Cases 6-8 | Sine wave, intensity: 0.1 g, frequency: 5, 10, and 15 Hz, respectively |
| Case 9 | WN-3; intensity: 0.05 g |
| Cases 10-12 | Sine wave, intensity: 0.2 g, frequency: 5, 10, and 15 Hz, respectively |
| Cases 13 | WN-4; intensity: 0.05 g |
| Cases 14-16 | Sine wave, intensity: 0.3 g, frequency: 5, 10, and 15 Hz, respectively |
| Case 17 | WN-5; intensity: 0.05 g |
| Cases 18-20 | Sine wave, intensity: 0.4 g, frequency: 5, 10, and 15 Hz, respectively |
| Case 21 | WN-6; intensity: 0.05 g |
| Cases 22-24 | Sine wave, intensity: 0.5 g, frequency: 5, 10, and 15 Hz, respectively |
| Case 25 | WN-7; intensity: 0.05 g |
| Cases 26-28 | Sine wave, intensity: 0.6 g, frequency: 5, 10, and 15 Hz, respectively |
| Case 29 | WN-8; intensity: 0.05 g |
| Cases 30-32 | Sine wave, intensity: 0.7 g, frequency: 5, 10, and 15 Hz, respectively |
| Case 33 | WN-9; intensity: 0.05 g |
| Cases 34-36 | Sine wave, intensity: 0.8 g, frequency: 5, 10, and 15 Hz, respectively |

Note: vertical-direction excitation with 15 s excitation duration adopted in this study; WN-1 means white noise and No.

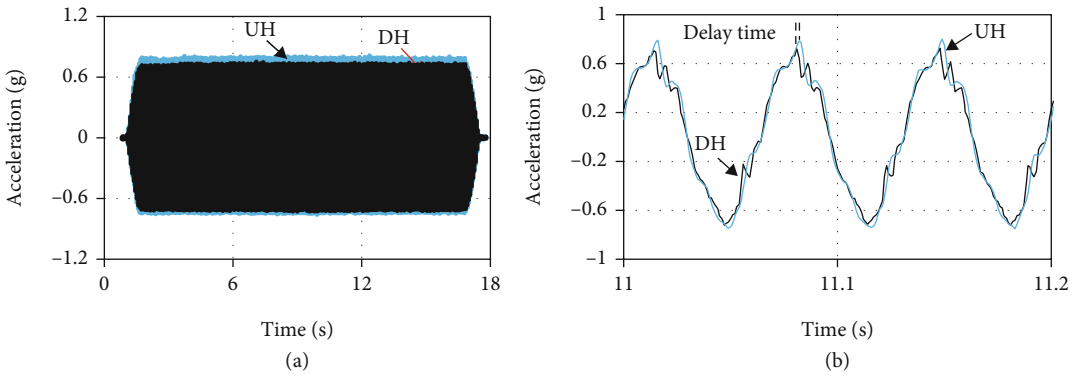


Figure 11: Time series data of acceleration.

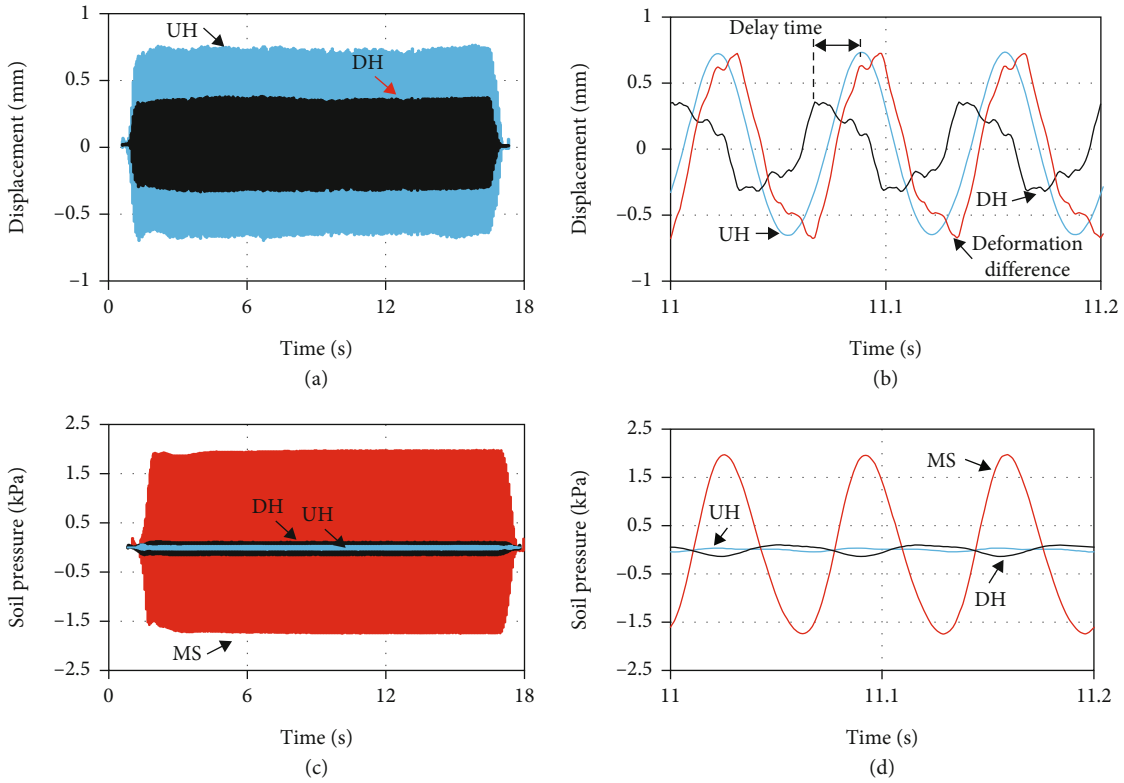


Figure 12: Time series data of (a) displacement and (c) soil pressure. Close-up views of displacement (b) and soil pressure (d).

the calculated elasticity modulus value of layer MS is 0.47 MPa. According to the early test results, layer MS cannot stand the weight of the upper layer under the elasticity modulus. For the abovementioned reasons, the similarity coefficients of fault and dolomite are different in this study.

Some fundamental factors in dynamic test such as length ($L$), gravity ($g$), stress ($\sigma$), and acceleration ($a$) have been taken into consideration. At last, the similarity coefficients of $\rho$, $E$, and $t$ of the dolomite layer are 1, 200 ,and 10, respectively, and those of fault are 1, 100, and 10. Scale factors of the study are given in Table 1.

*3.3. Materials.* Parameters of test model have been determined, and suitable materials have been chosen according to the similarity laws of Table 1. Materials of layer MS are made of quartz sand (60 meshes), clay (325 meshes), liquid paraffin, gypsum, and water at the ratio of 17 : 80 : 2 : 1 : 17.02 (the mixing amount of water refers to the percentage of water in the total mass of material). And materials of layers DH and UH contain barite powder, quartz sand (40 meshes), gypsum, iron powder, water, and glycerol at the ratio of 37.5 : 37.5 : 7 : 18 : 11.48 : 2.3 (the mixing amounts of water and glycerol refer to their percentages to the total mass of material). The physical and mechanical parameters of fault and dolomite prototypes obtained by test and model material are shown in Table 2. It should be noted that not all the factors meet the similarity law of the 1 g gravity field in our tests. For example, the densities of the fault prototype and model

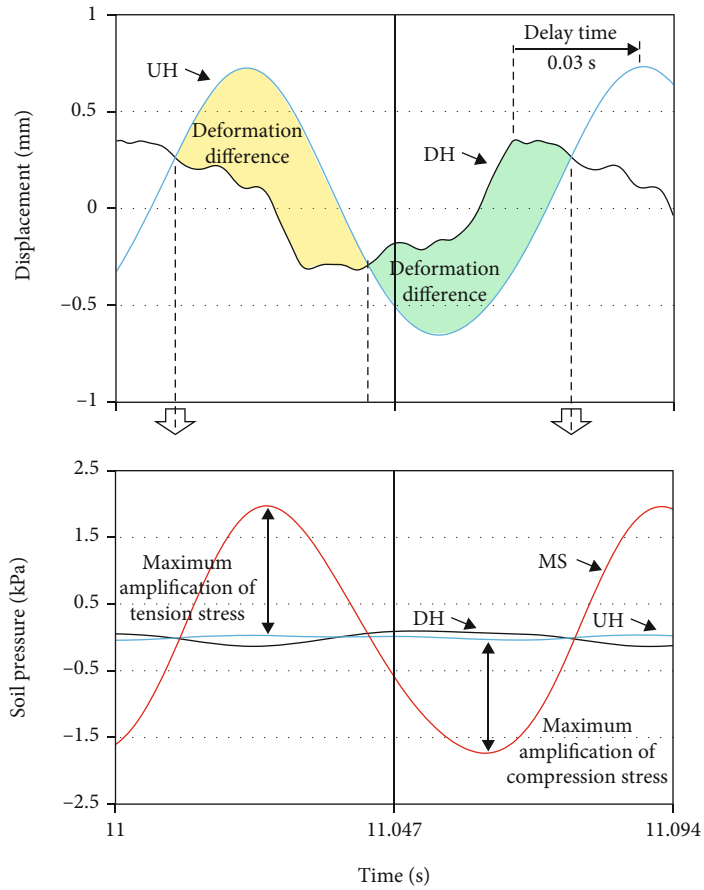


Figure 13: Close-up views of displacement and soil pressure responses at a same period.

test are still different, even though elasticity modulus meets the similarity law. Only some key parameters having remarkable influence on test results are chosen to meet the similarity law.

Dynamic triaxial test is done under the confining pressure of 50 kPa and initial axial pressure of 20 kPa. Test pressure increases by 5 kPa for every level, and there are 10 levels in total. And vibrating frequency per level is 100 times. By the test, the dynamic deformation, dynamic elasticity modulus, and damping ratio characteristics of model materials are obtained. It is known from Figure 7 that the deformation of fault model material in dynamic load cycle is irreversible. When the axial pressure change amplitude is greater than 60 kPa, the axial strain of the fault model material is 0.4%, including 80% of plastic strain (Figure 7(a)). For the dolomite model material, the axial strain is only about 0.05%, including plastic strain of no more than 10% (Figure 7(b)) under the pressure change amplitude of 100 kPa. At the beginning of vibration, the elasticity modulus of dolomite model material is about 30 times the fault material. The elasticity moduli of both materials reduce with the increase of vibration frequency. At the strain of 1%, the fault material's elastic modulus reaches a very small value, and the elasticity modulus of dolomite model material is 120 times the fault model material (Figure 7(c)). At the beginning of the test, the initial damping ratio ($\lambda_d$) of fault model material is twice the dolomite model material and increases faster than the dolomite model material. At the strain of 1%, $\lambda_d$ of fault model material is 3 times the dolomite model material (Figure 7(d)). It can be found that the fault model material is featured with low elasticity modulus, which is far lower than the dolomite model material.

*3.4. Model Construction.* For a similar model, the smaller the geometric similarity coefficient, the larger the model size, and the higher the test precision. The maximum length, maximum width, and maximum thickness of the DGB landslide body are about 2.8 km, 1.3 km, and 0.4 km, respectively. If it takes 200 as the similarity coefficient of dolomite, the size of the whole model is 14 m × 16.5 m × 2 m (length × width × height) (excluding the fault thickness). One unit is taken into account in our tests, and the size is determined as 0.64 m × 0.345 m × 0.6 m (length × width × height) (Figure 8(a)).

A rigid model box is applied to the test. A 50 mm-thick steel plate is added at the bottom of the box. As the steel plate is smooth, rows of screw-thread steel with a diameter of 2 cm are welded parallel at the spacing of 5 cm to improve the adhesion strength between the bottom face of the model and the steel plate.

*3.5. Measurement.* Dynamic strain type earth pressure sensor in the size of $\varphi$ 30 × 15 mm and precision of 0.1 kPa is applied. Fix the earth pressure sensor or acceleration sensor at the center of a one mm-thick lead sheet with the side edge length of 3 cm and bury it flatly into the model (Figures 8(a) and 8(b)). Monitor the displacement with a pressure lever-type displacement sensor with a precision of 0.05 mm. A set of self-made displacement monitoring devices (Figure 8(c)) by fixing the displacement sensor to the bottom steel plate of the model box with rigid magnetic seat and manipulator arm is used to measure the relative displacement between the model box and the steel plate at bottom. Put the probe of displacement sensor on the embedded right-angle iron sheet with one face horizontal and one face vertical. The vertical face is for horizontal displacement measurement (Figure 9(a)), which is not required in this paper. Put the displacement sensor probe vertically on the horizontal face of the right-angle iron sheet to measure the vertical displacement (Figure 9(b)). The earth pressure sensor, acceleration sensor, and displacement sensor were embedded in layers UH and DH, but only the earth pressure sensor and acceleration sensor were embedded in layer MS.

*3.6. Wave Input.* The sine wave is taken as the input wave during the test. Qingping seismic station (10 km southeast of the landslide) is the nearest seismic station around the DGB landslide. The earthquake accelerations in three directions of the Wenchuan earthquake are 0.84 g (E–W), 0.82 g (N–S), and 0.64 g (up-down). Based on the earthquake records of the Qingping seismic station, the maximum amplitude of sine wave for the test is set at 0.8 g. As the Fourier spectrum analysis of the Qingping seismic station shows that the earthquake frequency is mainly within 30 Hz, at 10 Hz in most cases, the sine wave frequency levels are set at 5 Hz, 10 Hz, and 15 Hz for the test. The monitored earth pressure, acceleration, and displacement wave signal main frequency are shown in Figure 10. Although the Wenchuan earthquake lasted for 160 s, the intensity reached the peak around 37–55 s. Therefore, the input wave duration for the test is set at 15 s. More details about the test can be found in Table 3.

*3.7. Test Process.* Preheat instrument for 0–2 s before test and then load sine wave by three steps: step I, increase amplitude to a preset level (2–3.5 s) gradually; step II, vibrate steadily (3.5–14.5 s); and step III, decrease amplitude to 0 (14.5–16 s) gradually. Input amplitude is within the range of 0.1–0.8 g, and the input frequencies are 5 Hz, 10 Hz, and 15 Hz. The first 0.05 g white noise scanning (WN1) needs to be done before test, then once every 3 cases. Nine times of scanning are required throughout the test (WN1–WN9). White noise is used to analyze the change in natural vibration parameters (elasticity modulus and damping ratio) of the model. The calculation equations of the elasticity modulus and damping ratio are shown as follows:

$$T_{xy}(f) = \frac{P_{yx}(f)}{P_{xx}(f)}, \quad (1)$$

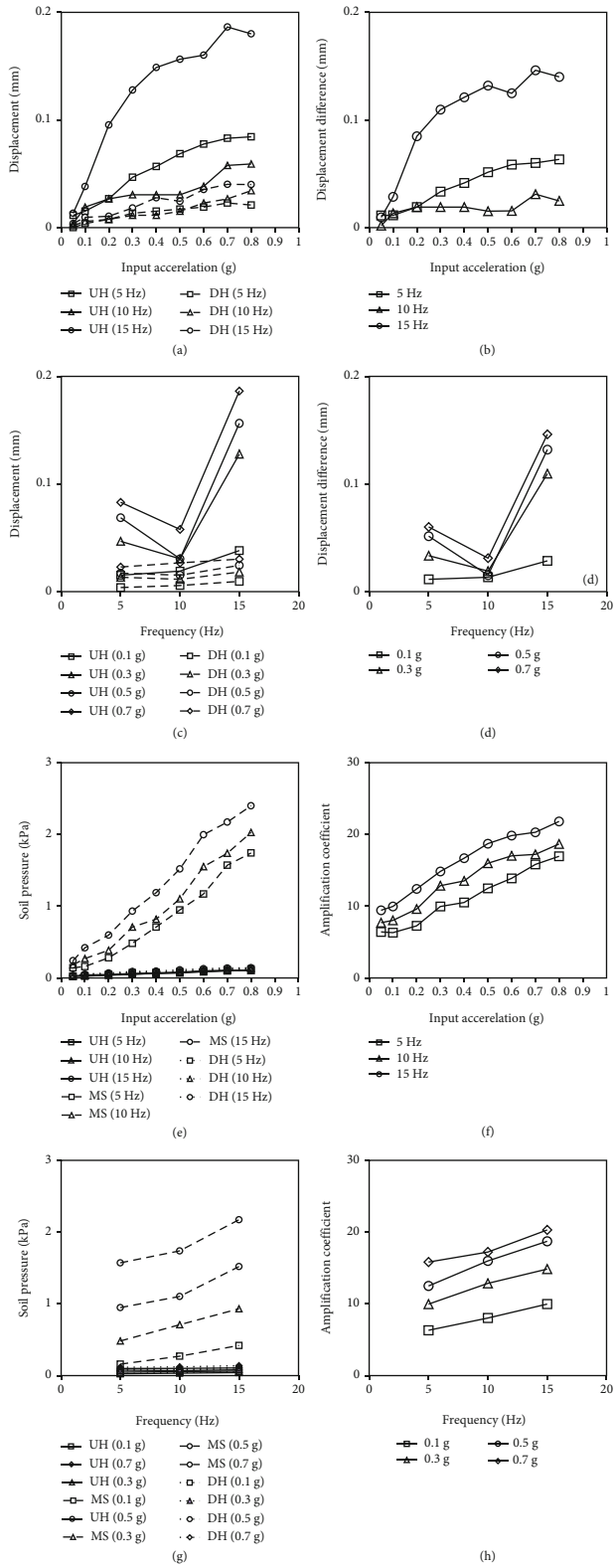


FIGURE 14: Seismic responses data of the model. (a) Displacement, (b) displacement difference, (e) soil pressure, and (f) amplification coefficient of soil pressure under input excitations of 0.05 g, 0.1 g, 0.2 g, 0.3 g, 0.4 g, 0.5 g, 0.6 g, 0.7 g, and 0.8 g. (c) Displacement, (d) displacement difference, (g) soil pressure, and (h) amplification coefficient of soil pressure under input frequencies of 5 Hz, 10 Hz, and 15 Hz.

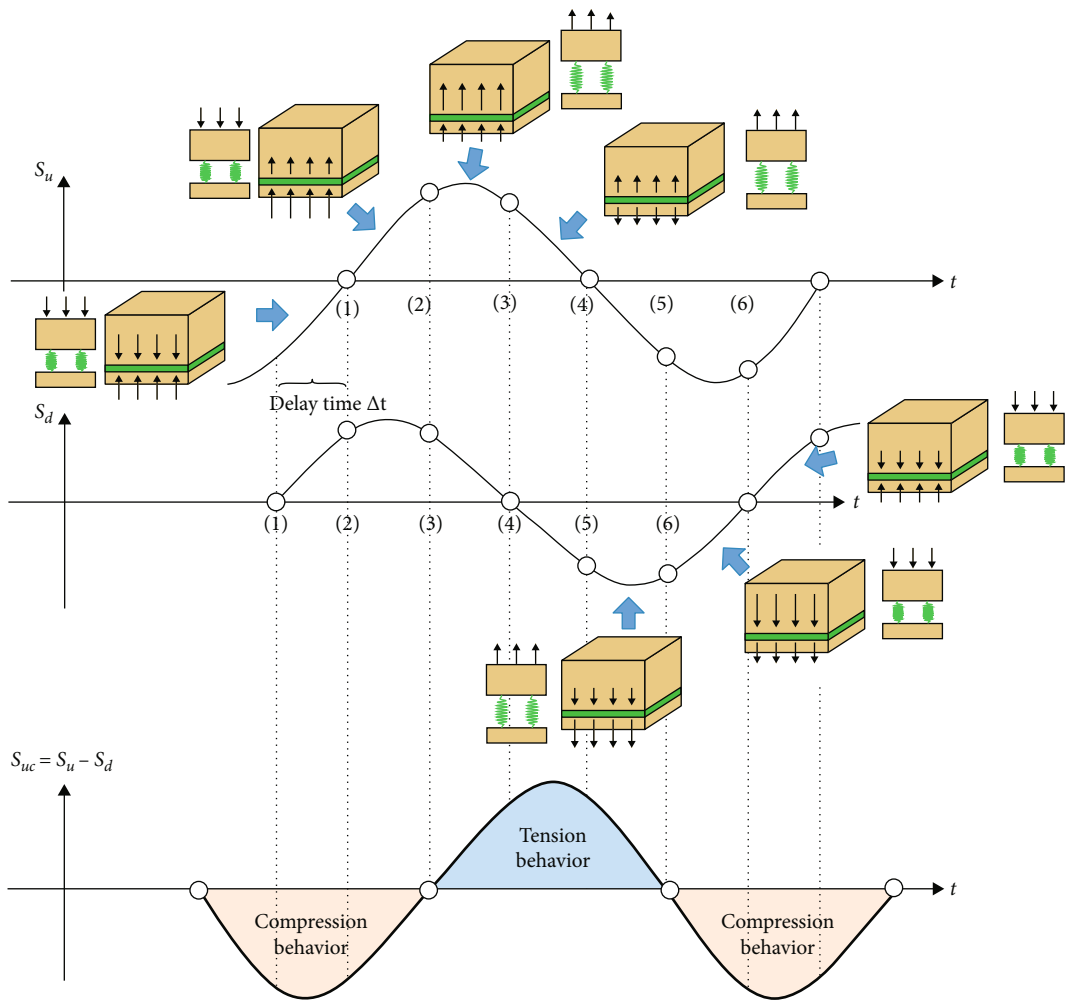


FIGURE 15: Stress amplification in the weak layer triggered by the generation of the delay time between the layers UH and LH. The compression and tension deformations of the weak layer are shown by spring models. The arrows indicate the direction and magnitude of movement.

wherein $T_{xy}(f)$ is the transfer function between input white noise signal $x$ and output white noise signal $y$, $P_{yx}(f)$ is the autocorrelation spectral density function between $x$ and $y$, and $f$ is the frequency argument in transfer function. In the transfer function-frequency relation curve, the frequency at the peak is the natural vibration frequency of the model. Calculate damping ratio by half-power bandwidth method:

$$\lambda = 0.5 * \frac{f_2 - f_1}{f_0}. \tag{2}$$

$f_0$ is the natural frequency calculated by transfer function, and $f_1$ and $f_2$ are corresponding frequencies at the 0.5 time peak positions on both sides of peak of the transfer function imaginary part-frequency relation curve.

The natural vibration frequency and damping ratio calculated by taking the acceleration sensor records under layer MS as the input signal and above layer MS as the output signal can reflect the characteristic changes of layer MS. If the change in natural vibration parameters is great (or change in natural vibration frequency or damping ratio is greater than 3%), it is deemed that layer MS is badly damaged at the moment, and the test needs to be terminated.

*3.8. Data Processing.* The resonance effect will not occur as the natural vibration frequencies under all working conditions obtained by Equation (2) are all greater than the input wave frequency of the paper. Changes in natural vibration frequency and damping ratio of model are only 1%. Peak acceleration $a$, peak displacement $s$, and peak earth pressure $\sigma$ are taken for test results analysis in this paper. If $S_u$ is the average peak displacement of layer UH in stable vibration stage (3.5–14.5 s) and $S_d$ is the average peak displacement of layer DH in stable vibration stage, $S_{uc}$ is displacement difference:

$$S_{uc} = S_u - S_d. \tag{3}$$

The earth pressure amplification coefficient describes the amplification of earth pressure of layer MS, which is as follows:

$$\xi_p = P_{ts} - P_{td}, \quad (4)$$

wherein $P_{ts}$ is the average peak earth pressure of layer MS in stable vibration stage and $P_{td}$ is the average peak earth pressure of layer DH in stable vibration stage. Positive and negative values of acceleration, respectively, represent the upward and downward vibrations of tested point. Positive and negative values of earth pressure, respectively, represent the pressure and tension. And positive and negative values of displacement, respectively, represent the tensile deformation and compressive deformation.

## 4. Results

Figures 11 and 12 show the test results of acceleration, displacement, and earth pressure collected at different monitoring points. Taking the case with 0.6 g and 15 Hz as an example, the test results of acceleration response of different monitoring points are shown in Figure 11. The peak acceleration of the layer DH is about 0.72 g, whereas the peak acceleration of layer UH is 0.8 g, which is amplified by 1.11 times in comparison with that of the layer DH (Figure 11(a)). There is a phase difference between the response signals of peak acceleration between the layers UH and DH, and the phase difference is about 0.002 s (Figure 11(b)). The test results of displacement response of different monitoring points are shown in Figures 12(a) and 12(b). The peak displacement of the layer DH ($S_u$) is 0.35 mm, and the peak displacement of the layer UH ($S_u$) is 0.74 mm, which is amplified by 2 times in comparison with that of the layer DH (Figure 12(a)). Similarly, there is also a phase difference between the response signals of peak displacement between the layers UH and DH, and the phase difference is about 0.03 s (Figure 12(b)). As shown in Figures 12(c) and 12(d), the peak earth pressures of the layers MS, UH, and DH are 1.98 kPa, 0.05 kPa, and 0.13 kPa, respectively. The peak earth pressure of the layer MS is 29.7 times and 14.8 times that of the layers UH and DH, respectively.

Figure 13 shows the data of displacement and earth pressure at the same time. When tensile deformation (positive displacement difference) is monitored by displacement sensor, the earth pressure curves of layers UH and DH are observed separation from each other, and tension force within layer MS is recorded. When compressive deformation (negative displacement difference) is monitored by displacement sensor, the compressive force within layer MS is recorded.

Figure 14(a) shows that the peak displacement of the layer UH increases nonlinearly with the increase of the input amplitude. When input amplitude is smaller than 0.5 g, the displacement peak of the layer UH increases faster with the intensifying of input wave, while the displacement peak of the layer UH increases slower once it exceeds 0.5 g. The peak displacement of the layer DH increases linearly with the increase of input amplitude, but the peak displacement of the DH layer is significantly smaller than that of the layer UH (Figure 14(a)). Taking the input frequency of 5 Hz as an example, the peak displacement of the layer UH is 3.10 to 4.21 times that of the DH layer. With the increase of input amplitude, the peak displacement difference between the layers UH and DH also gradually increases. Taking the input

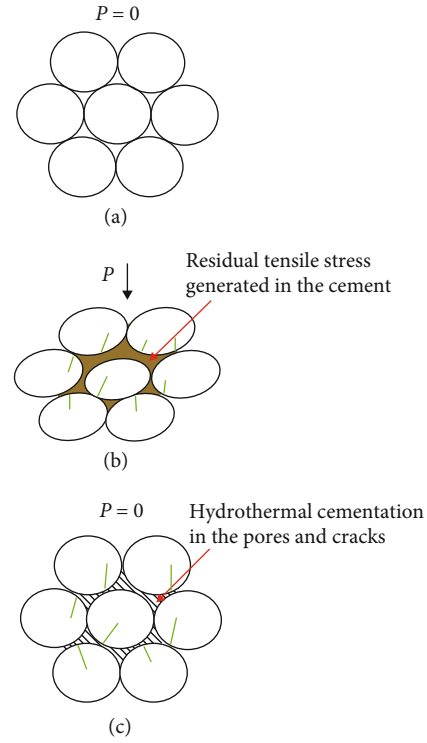


Figure 16: Unloading induced rock mass tension failure. (a) Original state without tectonic pressure ($P = 0$), (b) tectonic compressive pressure-induced fragmentation (green lines represent cracks) and hydrothermal cementation in the pores and cracks under the compressive pressure condition, and (c) residual tensile stress generated in the cement under unloading condition ($P = 0$).

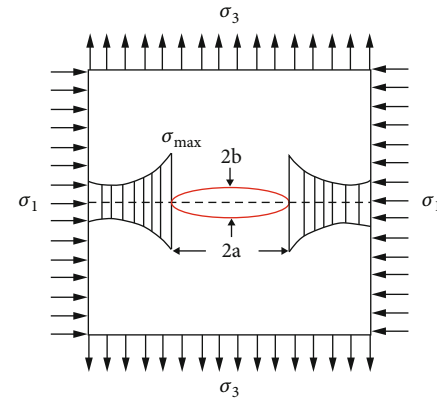


Figure 17: Tension force was concentrated at the ends of a horizontal crack under the vertical minimum principal stress ($\sigma_3$) and horizontal maximum principal stress ($\sigma_1$) conditions.

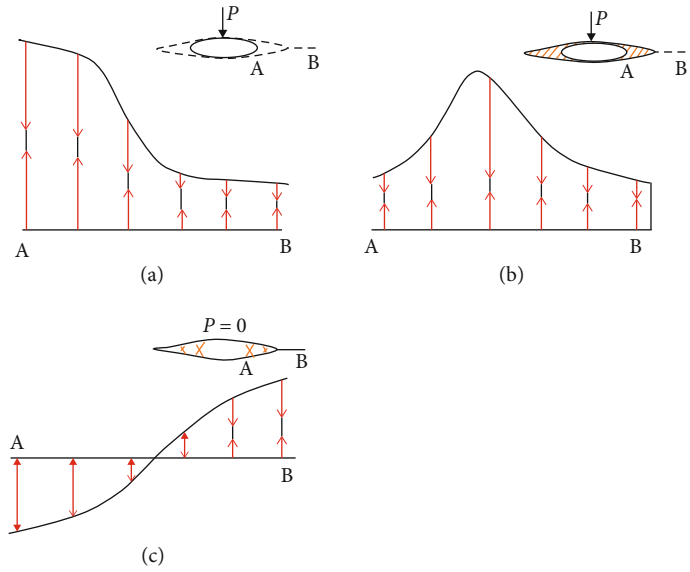


Figure 18: Fracture related to compressive stress. (a) A horizontal crack under compression stress ($P$). Compression stress is concentrated at point A (the end of the crack) due to $P$. (b) Rock mass at point A was crushed (slash filled area), and the stress concentration point is transferred toward point B. (c) Residual tensile stress is generated at point A (cross line filled area) due to unloading ($P = 0$).

frequency of 15 Hz as an example, the displacement difference increases from 0.03 to 0.15 mm (Figure 14(b)). Under different input wave frequencies, the peak displacement of the layer UH first decreases and then increases with the increase of the input wave amplitude. The peak displacement reaches the largest at the input wave frequency of 5 Hz, and the peak displacement is the smallest at the input wave frequency of 10 Hz (Figure 14(c)). The peak displacement of the layer DH increases slowly with the increase of input amplitude (Figure 14(c)). The displacement difference between the layers DH and UH is the smallest at 10 Hz and the largest at 15 Hz (Figure 14(d)).

Figure 14(e) shows that the peak earth pressure of the layers MS, UH, and DH increases linearly with the increase of the input amplitude, but the peak earth pressure growth rate of the layer MS is significantly higher than that of the layers UH and DH. Taking the input frequency of 5 Hz as an example, the growth rates of peak earth pressure of the layers MS, UH, and DH are 2.25, 0.11, and 0.13, respectively (Figure 14(e)). The calculation results of amplification coefficient of earth pressure ($\xi_p$) show that the amplification coefficient of peak earth pressure shows a linear growth trend with the increase of input amplitude (Figure 14(f)). The larger the frequency of the input wave, the larger the amplification coefficient of the peak earth pressure. For example, the amplification coefficient of input frequency of 15 Hz is 1.18 and 1.49 times that of input frequency of 5 Hz and 10 Hz, respectively (Figure 14(f)). The peak earth pressure of the layers MS, UH, and DH increases linearly with the input frequency, but the growth rates of the layers UH and DH are significantly lower than that of the layer MS (Figure 14(g)). Accordingly, the amplification coefficient of peak earth pressure also increases linearly with the increase of input frequency and reaches the maximum at 0.7 g (Figure 14(h)).

Based on the test results, six types of layer UH to layer DH relative movement modes (Figure 15) have been proposed, wherein $\Delta t$ refers to delay of time of the upper hard layer than that of the lower one.

(i) Type 1: lower hard layer moves upwards, while the movement of the upper hard layer is slower than the lower hard layer since the $\Delta t$. The lower hard layer hits the upper one and results in compressive stress amplification in the weak layer

(ii) Type 2: lower hard layer starts to slow down after reaching the upward moving peak speed. The upper hard layer is around the peak because of the generation of $\Delta t$. As the upper hard layer is moving faster than the lower one, the gap between them gets larger, and tension stress amplification is caused therefrom in the weak layer

(iii) Type 3: lower hard layer moves reversely (downwards), while the upper hard layer still moves in the original direction but slower; so, the distance between the upper and lower layers increases, and a tension stress amplification generates in the weak layer

(iv) Type 4: the speed of the lower hard layer reaches the peak, while the upper hard layer moves reversely but slower than the lower one; so, the distance between them increases, and a tension stress amplification occurs in the weak layer as a result

(v) Type 5: the downward movement of the lower hard layer slows down, while the downward speed of the upper hard layer reaches the peak; so, a compressive

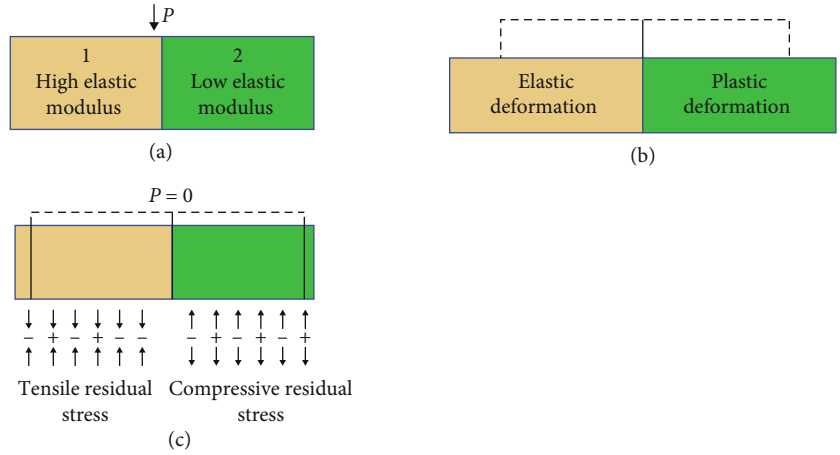


FIGURE 19: Fracture related to rebounding ability. (a) Rock is composed of two elastic modulus units. (b) Compression stress ($P$) is applied to the rock. (c) Residual tension force generated in the low elastic modulus unit during unloading ($P = 0$). Tensile stress is generated in the low elastic modulus unit.

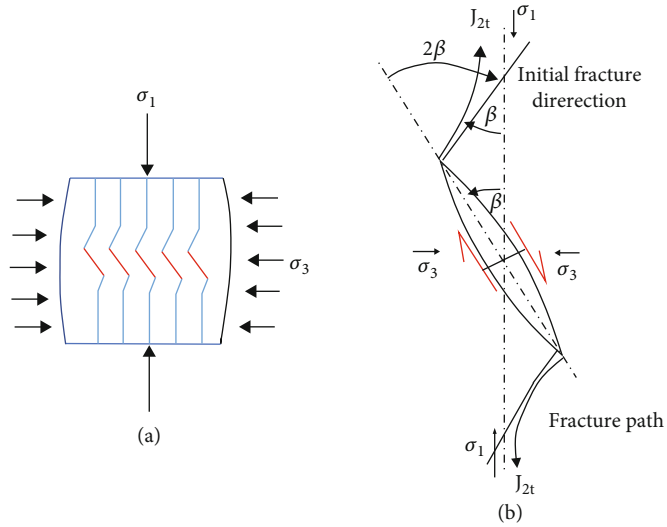


FIGURE 20: (a) Inclined crack (red lines) under vertical maximum principal stress ($\sigma_1$) and horizontal minimum principal stress ($\sigma_3$) conditions. The compression stress causes tension failure (green lines). (b) Close-up view of crack shows Griffith tensile fracture path ($J_{2t}$).

stress amplification is caused in the weak layer after the two layers have a crash

(vi) Type 6: lower hard layer moves reversely (upwards), while the upper one moves downwards. A compressive amplification is caused in the weak layer under the hedge function between the two hard layers

## 5. Discussion

*5.1. Cause of Stress Amplification in Bedding Fault.* The weak structural surfaces such as weak interlayer have a significant effect on the seismic response of slopes [37, 38]. In fact, the seismic response of rock slopes is the disturbance effect of waves propagating in the rock mass [39]. Wave propagation through the structural planes will cause obvious wave refraction and reflection effects [40], its reflection and transmission coefficients are both smaller than 1, and wave amplitude decays for the energy consumption caused by reflection and transmission. The degree of amplitude attenuation of the upper layer increases with the number of interfaces the incident seismic wave passes through, which is also known as the vibration-insulating effect for the upper layer [14]. Thicker and deeper buried weak layer is more prone to generate shock absorption. On the contrary, seismic amplification is observed, and the intensity of site ground motion amplification will be enhanced by the smaller wave velocity of the weak layer. In addition,


FIGURE 21: Fragmentation of the bedding fault rock mass. (a) Trench, (b) close-up view of the rock mass shows tension cracks, and (c) rock mass dilatation due to earthquake induced tension fracture.

the vertical and transverse stiffness of the weak layer also plays an important role in seismic amplification. These results have been used in the foundation seismic isolation of buildings [41].

Ground motion amplification and attenuation study are not the aim of this study, but the weak layer response which is important for slope stability. As the shear wave velocity of the hard layer materials could reach 3000 m/s, while that of the weak layer is only 200 m/s, an obvious time delay would be caused by the weak layer (Figures 11 and 12). A phrase difference was generated between the signals monitored from the upper hard layer and the lower hard layer. The time delay blocked uniform vibration between the upper and lower hard layers. The model in this condition can be simplified as a vibration system composed of the upper and lower rigid blocks and a spring connecting them as shown in Figure 6(c). Taking the lower hard layer for a reference, the 6 types of modes mentioned in the previous paragraph could be simplified into two types. One is that the upper hard layer moves downwards relative to the lower layer to cause compression amplification in the weak layer. The other is the "separation" between upper hard layer and lower hard layer to cause tension amplification in the weak layer.

*5.2. Effects of Tensile Stress Amplification.* During the active period of tectonic movement, fault rock mass was extruded and tensile fissures developed, which can be filled by hot fluid [42]. The fault rock mass will be unloaded when the compressive stress decrease during quiet period of tectonic activity, but the unloading will be restricted by the cement. Tensile stress will be generated on the cement, namely, the residual tensile stress (Figure 16). The tensile stress component of earthquake can couple with the residual tensile stress to cause large numbers of tensile fissures in bedding fault during earthquake, which may explain why the micro-


FIGURE 22: Fragmentation of beddrock. (a) Borehole cores, (b) tension crack surface (rough surface), and (c) shear fracture surface.

images of the sample taken from bedding fault of DGB landslide presents high density of fresh fractures [28]. These fresh fractures show brittle fracture propagation, which presents evidence that the occurrence of tensional stress motion [43, 44].

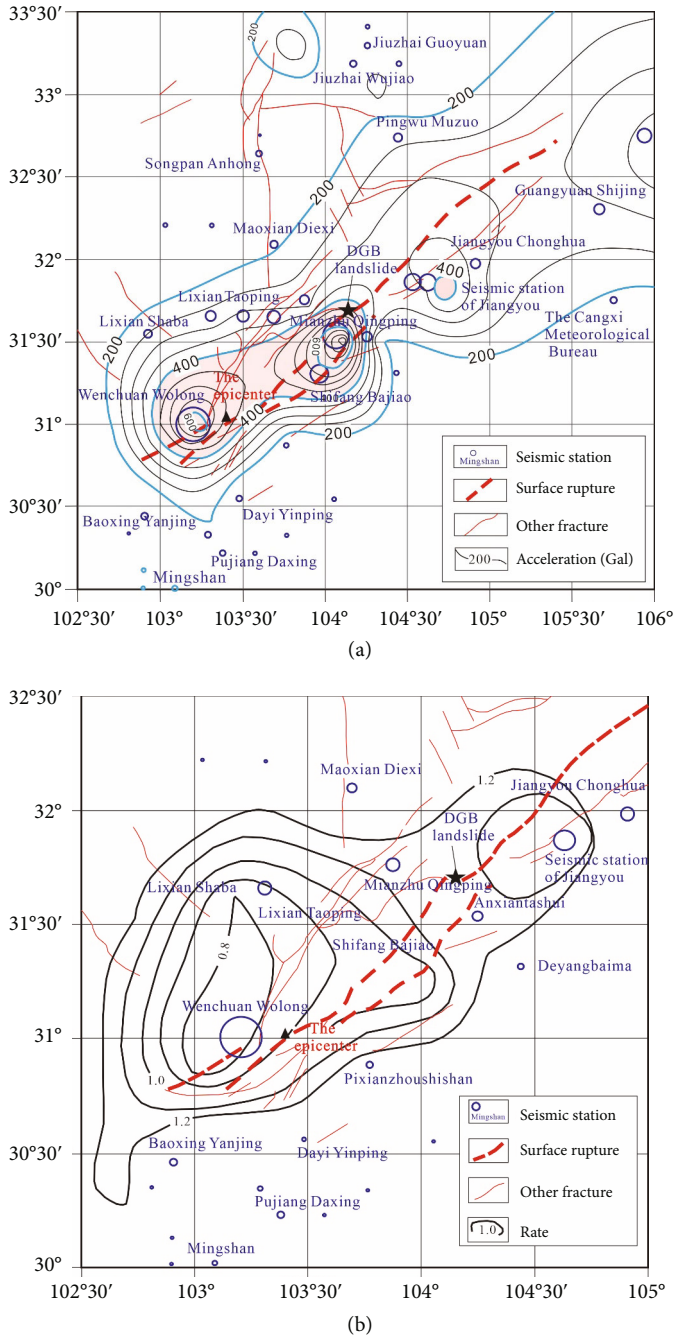


Figure 23: (a) Contour maps of vertical seismic acceleration (UD) and (b) seismic acceleration ratio (south–north acceleration to UD) of the Wenchuan earthquake.

The $\sigma_1$ and $\sigma_3$ represents the maximum and minimum main stresses (Figure 17). If $\sigma_1 + 3\sigma_3 \geq 0$, tensile stress $\sigma_3$ plays a leading role in rock breaking. If $\sigma_3 = -S_t$ ($S_t$ refers to the tensile resistance of rock), rock is broken. The fissure developed at this time is nearly parallel to the tensile stress, which means that nearly horizontal fissure with gentle dip angle is developed (Figure 17). As the tensile resistance of rock is much smaller than its compressive resistance, such tensile failure is easy to occur. These kinds of tensile stress amplifications we observed in our tests will undoubtedly increase these kinds of rock fragmentation and enhance the probability of slope instability.

*5.3. Effects of Compressive Stress Amplification.* Under the effect of compressive stress $P$, the preexisted fissures in rock mass would produce concentrated compressive stress at the fissure tips. Stress of point A is greater than that of point B as shown in Figure 18(a). If the stress exceeds rock mass

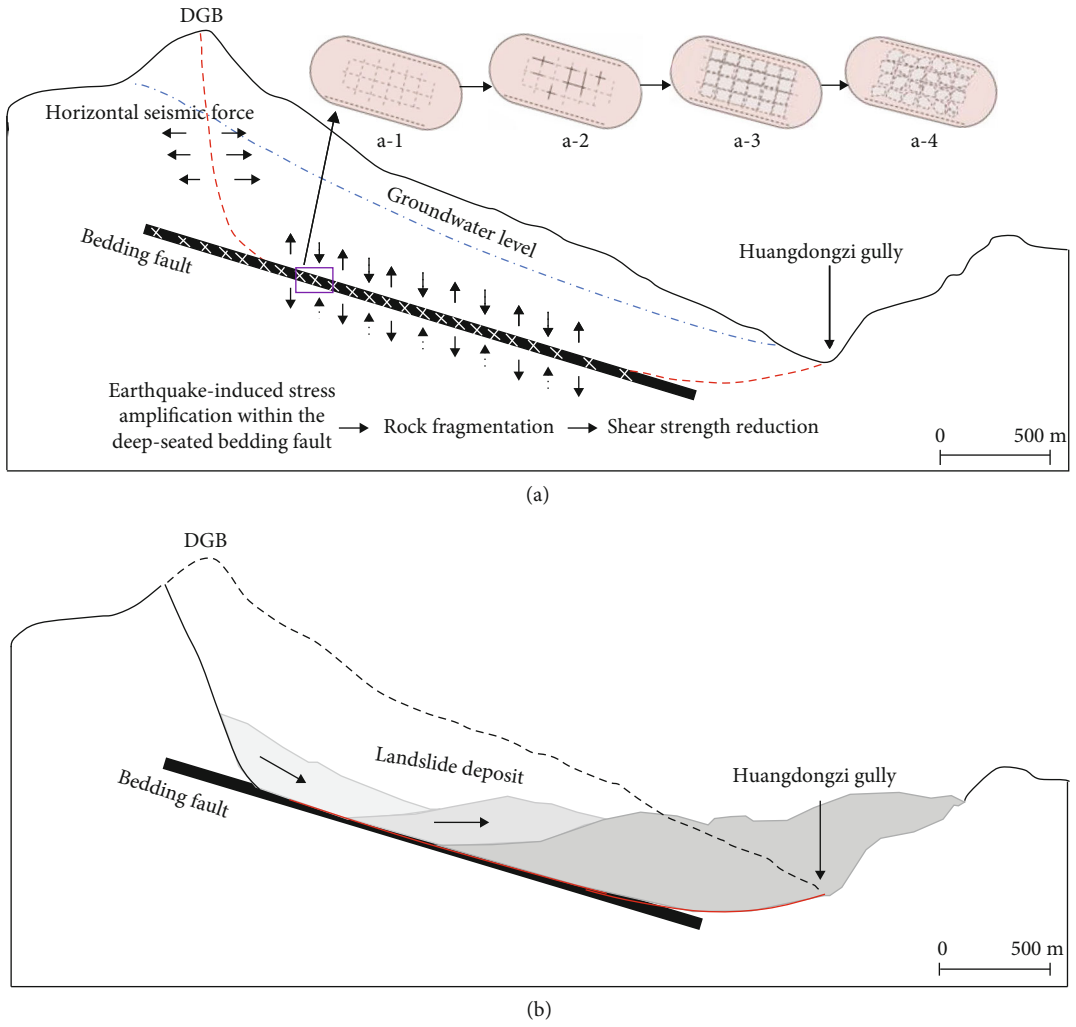


Figure 24: A formation model of the DGB landslide considering the earthquake-induced stress amplification. (a) Horizontal seismic force-induced tension failure in the slope. Meanwhile, earthquake-induced stress amplification within the deep-seated bedding fault resulted in rock fragmentation. Friction on the basal surface reducted due to the rock mass fragmentation and the landslide was initiated. (b) The movement of the landslide body was constrained on the bedding fault.

strength, fissure tips will have plastic deformation or fragmentation. The concentrated stress will move inwards then, namely, from point A to point B (Figure 18(b)). The resilience of fissure ends is weakened during unloading, while the elasticity modulus of the integrate rock mass is still high, and residual tensile stress and compressive stress will develop at the two points. In Figure 18(c), tensile stress is developed at point A.

The rock mass is inhomogeneous in both material and stress. As fault is composed of inhomogeneous rock mass developed after many times of tectonic movements [28, 42], it has closely connected units with different dielectric properties (Figure 19(a)). Under compressive stress conditions, high-elasticity modulus unit generates elastic stress under pressure, while low-elasticity modulus unit can generate plastic deformation beyond that (Figure 19(b)). After stress release, residual compressive and tensile stresses will generate at both units for the different resilience (Figure 19(c)). Tensile failure will occur if the residual tensile stress reaches the material tensile resistance.

For the preexisted fissure with moderate dip angle (Figure 20(a)), under compressive stress condition, the strongest tensile stress is located at the end of the fissure with the intersection angle $\beta$ with the main compressive stress at 30°–40° when $\sigma_1 + 3\sigma_3 \le 0$ based on the Griffith criterion [45]. When $(\sigma_1 - \sigma_3)^2/(\sigma_1 + \sigma_3) = 8S_t$, rock mass is broken. The fissure expands into branches ($J_{2t}$) in the broken rock mass area. The intersection angle between the initial direction of fissure branch and the original long axis direction of the fissure is about $2\beta$. Then, the fissure is gradually parallel to the maximum main compressive stress. Finally, a large-dip angle fissure nearly vertical to the rock mass is developed (Figure 20(b)). The tensile stress component of earthquake can couple with this compressive stress amplification-induced residual tensile stress to make the fissure expand quickly and enhance the probability of slope instability.

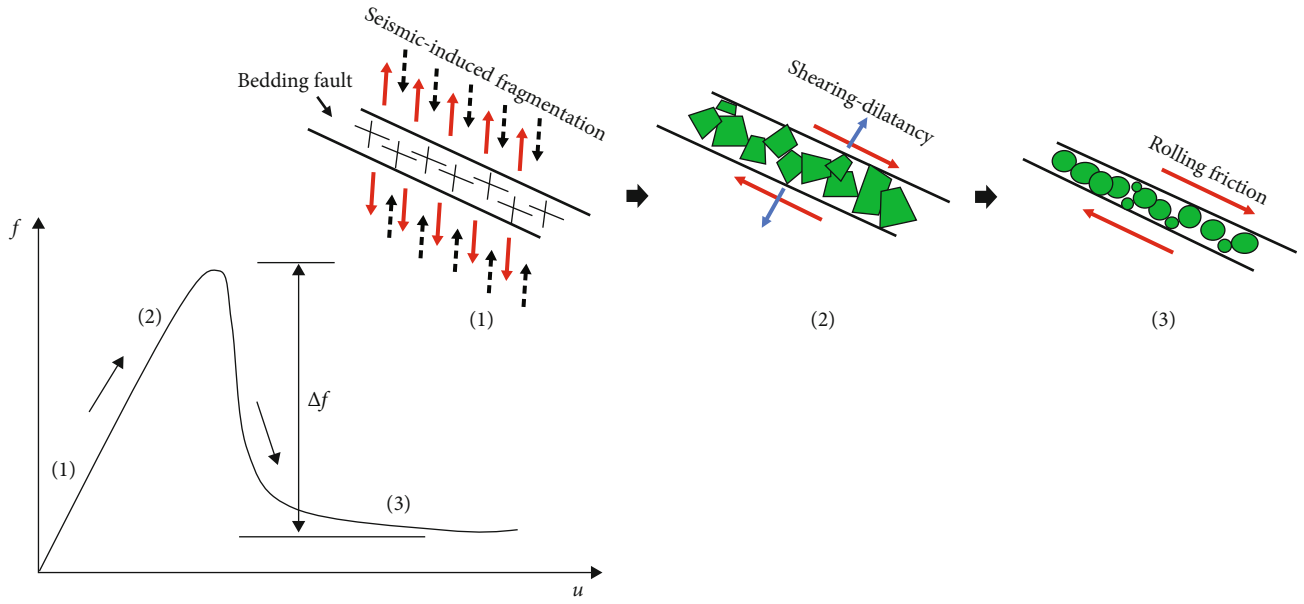


FIGURE 25: Variation of the friction on the basal layer corresponded to rock mass fragmentation. (1) Seismic-induced fragmentation. (2) Shearing-dilatancy induced friction increase at the first stage. (3) Then, friction was weakened rapidly due to rolling movement.

*5.4. Applications of the DGB Landslide.* Since the occurrence of Daguangbao (DGB) landslide, its seismic failure mechanism has been widely concerned [34, 42, 46]. Some hypotheses were put forward about the initiation mechanism of the DGB landslide. However, the earthquake-induced stress amplification within the potential sliding zone was not taken into consideration in the previous studies. In this study, a great deal of earthquake-induced fissures has been found on the field (Figures 21 and 22). The horizontal and vertical fissures under sliding surface are shown in Figures 21(b) and 21(c). The tensile and shear ruptures with moderate dip angle can be found in Figures 22(b) and 22(c). We proposed that the compression and tension stress amplification of the weak layer during earthquake can induce these kinds of ruptures and result in the sudden loss of stability of the DGB landslide.

The peak ground accelerations (PGA) in EW, SN, and UD directions recorded by the seismic station 10 km from DGB landslide are 0.623 g, 0.824 g, and 0.803 g [47], respectively, all of which are at high level. The PGA ratio (SN to UD) in DGB landslide area is smaller than 1.2 (Figure 23), which means that the vertical seismic acceleration is high. Under the effect of vertical seismic force, stress amplification in the bedding fault of the DGB Mountain will occur (Figure 24(a)) and result in the fragmentation of the cemented fault rock mass, as shown in Figures 24(a)-1–a-4. Fragmentation of rock mass will reduce its peak shear strength, making the landslide much easier to be launched [28]. Landslide mass deposited in the valley ahead (Figure 24(b)). In the landslide moving process, the edges and corners of the fragmented rock blocks were quickly rounded. And then, it produced a force of rolling friction which led to a significant decrease in friction from peak to residual state. On this basis, the landslide will move ahead at a relatively low friction coefficient (Figure 25) to improve its movement ability.

However, the seismic failure of rock slopes occurs gradually with the increase in the earthquake energy, which is an evolution process instead of an instantaneous abrupt state [40, 48]. In particular, seismic failure process of slopes containing complex geological structures has a cumulative seismic effect [49, 50]. Therefore, one earthquake may not result in slope instability but can lead to a change in shear displacement for the short action time, but the fault failure can be caused by the stress amplification due to the fragmentation accumulated under the conditions of several times of earthquake. Once the critical permanent displacement is reached, or some locking sections in shear face are broken through, the shear strength will be significantly weakened, and the final failure of slope will occur. Some limitations of this study should be noted. The difference between fault elasticity modulus and fault thickness is not taken into consideration in this study. Our model is scaled down, and the similarity rates of dolomite layer and weak layer are different. In addition, the influence of horizontal seismic force is ignored in this study as well, which needs attention while applying the results.

## 6. Conclusion

Taking DGB landslide as the research object, a series of shaking table model tests are carried out in this study. The embedded sensors are used to obtain the dynamic response of the model with the weak layer, focusing on the seismic behavior of the bedding fault (i.e., the weak interlayer). The test results show that the peak displacement of the lower hard layer (i.e., layer DH) is much smaller than that of the overlying hard layer (i.e., the layer UH), and the peak earth pressure within the soft layer (i.e., the layer MS) is significantly larger than that of the lower hard layer. The seismic wave propagates in the weak layer will produce an obvious

time delay, resulting in a significant phase difference in deformation between the upper hard layer and lower hard layer. The incompatible deformation-induced stress amplification in the weak layer shows two different modes: one is the compressive stress amplification when the upper hard layer moves downward relative to the lower hard layer, and the other is tension stress amplification when the upper hard layer moves upward relative to the lower hard layer. This study highlights the contribution of earthquake-induced stress amplification to the failure of fractured rock mass in fault. Numerous new fractures with low- and steep-dip angles in the bedding fault observed at the landslide site provide field evidence of seismic damage caused by stress amplification. Finally, we propose that the stress amplification of deep-seated faults may cause the rapid decline of the shear strength of faults and the sudden initiation of landslides.

## Data Availability

The data supporting the results of the study have been shown in the tables and figures.

## Additional Points

*Highlights*. Physical model tests are used to evaluate the deformation behavior of slope with a deep-seated bedding fault during earthquake. Stress in deep-seated bedding fault is amplified during seismic shaking. Stress amplification in bedding fault caused landslide initiation through fault rock refragmentation.

## Conflicts of Interest

The authors declare no conflicts of interest.

## Acknowledgments

This study was partially supported by the National Science Foundation of China (Nos. 41907254 and 41931296), the State Key Laboratory of Geohazard Prevention and Geoenvironment Protection Independent Research Project (SKLGP2021Z014), National Key R&D Program of China (No. 2017YFC1501002), and Funds for Creative Research Groups of China (No. 41521002).

## References

[1] K. J. Chang, A. Taboada, and Y. C. Chan, "Geological and morphological study of the Jiufengershan landslide triggered by the Chi-Chi Taiwan earthquake," *Geomorphology*, vol. 71, no. 3–4, pp. 293–309, 2005.

[2] X. J. Pei, S. H. Cui, L. Zhu, H. Wang, L. G. Luo, and X. Zhang, "Sanxicun landslide: an investigation of progressive failure of a gentle bedding slope," *Natural Hazards*, vol. 111, no. 1, pp. 51–78, 2021.

[3] S. Zhang, Q. Xu, and Z. M. Hu, "Effects of rainwater softening on red mudstone of deep-seated landslide, Southwest China," *Engineering Geology*, vol. 204, pp. 1–13, 2016.

[4] Z. L. Zhang, T. Wang, S. R. Wu, H. M. Tang, and C. Y. Liang, "The role of seismic triggering in a deep-seated mudstone landslide, China: historical reconstruction and mechanism analysis," *Engineering Geology*, vol. 226, pp. 122–135, 2017.

[5] J. Cao, Z. Zhang, C. Z. Wang, J. F. Liu, and L. L. Zhang, "Susceptibility assessment of landslides triggered by earthquakes in the Western Sichuan plateau," *Catena*, vol. 175, pp. 63–76, 2019.

[6] F. C. Dai, C. Xu, X. Yao, L. Xu, X. B. Tu, and Q. M. Gong, "Spatial distribution of landslides triggered by the 2008 Ms 8.0 Wenchuan earthquake, China," *Journal of Asian Earth Sciences*, vol. 40, no. 4, pp. 883–895, 2011.

[7] X. M. Fan, G. Scaringi, Q. Xu et al., "Coseismic landslides triggered by the 8th august 2017 Ms 7.0 Jiuzhaigou earthquake (Sichuan, China): factors controlling their spatial distribution and implications for the seismogenic blind fault identification," *Landslides*, vol. 15, no. 5, pp. 967–983, 2018.

[8] T. Gorum, X. M. Fan, C. J. Westen et al., "Distribution pattern of earthquake-induced landslides triggered by the 12 may 2008 Wenchuan earthquake," *Geomorphology*, vol. 133, no. 3-4, pp. 152–167, 2011.

[9] C. Xu, X. W. Xu, and J. B. H. Shyu, "Database and spatial distribution of landslides triggered by the Lushan, China mw 6.6 earthquake of 20 April 2013," *Geomorphology*, vol. 248, pp. 77–92, 2015.

[10] M. Chigira, X. Y. Wu, T. Inokuchi, and G. H. Wang, "Landslides induced by the 2008 Wenchuan earthquake, Sichuan, China," *Geomorphology*, vol. 118, no. 3-4, pp. 225–238, 2010.

[11] S. Cui, Q. Yang, L. Zhu, X. Pei, S. Wang, and J. Liang, "The role of tectonic discontinuities in triggering large seismic landslides," *Lithosphere*, vol. 2022, Article ID 3196788, 23 pages, 2022.

[12] J. Luo, X. J. Pei, S. G. Evans, and R. Q. Huang, "Mechanics of the earthquake-induced Hongshiyan landslide in the 2014 Mw 6.2 Ludian earthquake, Yunnan, China," *Engineering Geology*, vol. 251, pp. 197–213, 2019.

[13] L. Zhu, S. H. Cui, X. J. Pei, S. Y. Wang, S. He, and X. X. Shi, "Experimental investigation on the seismically induced cumulative damage and progressive deformation of the 2017 Xinmo landslide in China," *Landslides*, vol. 18, no. 4, pp. 1485–1498, 2021.

[14] L. M. Fan and N. Li, "Transmission model of weak intercalation and its vibration isolation properties," *Chinese Journal of Rock Mechanics and Engineering*, vol. 24, no. 14, pp. 2456–2462, 2005.

[15] H. X. Liu, Q. Xu, F. Zhou, Z. Yang, and F. Wang, "Shaking table test for seismic responses of sloes with a weak inter layer," *Chinese Journal of Rock Mechanics and Engineering*, vol. 34, no. 5, pp. 994–1005, 2015.

[16] Z. L. Chen, X. Hu, and Q. Xu, "Experimental study of motion characteristics of rock slopes with weak intercalation under seismic excitation," *Journal of Mountain Science*, vol. 13, no. 3, pp. 546–556, 2016.

[17] H. X. Liu, T. Qiu, and Q. Xu, "Dynamic acceleration response of a rock slope with a horizontal weak interlayer in shaking table tests," *PLoS One*, vol. 16, no. 4, article e0250418, 2021.

[18] Z. L. Chen, X. Hu, and X. B. Bu, "Effect of weak intercalation on failure mode of rock slopes under seismic excitation," *Natural Hazards*, vol. 105, no. 1, pp. 363–381, 2021.

[19] Q. Chen, H. Cheng, Y. H. L. Yang, G. X. Liu, and L. Y. Liu, "Quantification of mass wasting volume associated with the

giant landslide Daguangbao induced by the 2008 Wenchuan earthquake from persistent scatterer InSAR," *Remote Sensing of Environment*, vol. 152, pp. 125–135, 2014.

[20] Y. P. Yin, W. M. Zheng, X. C. Li, P. Sun, and B. Li, "Catastrophic landslides associated with the M 8.0 Wenchuan earthquake," *Bulletin of Engineering Geology and the Environment*, vol. 70, no. 1, pp. 15–32, 2011.

[21] Y. B. Zhang, G. Q. Chen, L. Zheng, Y. G. Li, and J. Wu, "Effects of near-fault seismic loadings on run-out of large-scale landslide: a case study," *Engineering Geology*, vol. 166, pp. 216–236, 2013.

[22] W. F. Zhang, R. Q. Huang, and X. J. Pei, "Analysis on kinematics characteristics and movement process of Daguangbao landslide," *Journal of Engineering Geology*, vol. 23, no. 5, pp. 866–885, 2015.

[23] Y. B. Zhang, J. Zhang, G. Q. Chen, J. X. Zhao, L. Zheng, and Y. G. Li, "Effects of vertical seismic force on initiation of the Daguangbao landslide induced by the 2008 Wenchuan earthquake," *Soil Dynamics and Earthquake Engineering*, vol. 73, pp. 91–102, 2015.

[24] J. H. Wu, T. N. Do, C. H. Chen, and G. Wang, "New Geometric Restriction for the Displacement–Constraint Points in Discontinuous Deformation Analysis," *International Journal of Geomechanics*, vol. 17, no. 5, 2016.

[25] X. J. Pei, R. Q. Huang, S. H. Cui, Y. Du, and W. F. Zhang, "The rock mass cataclastic characteristics of Daguangbao landslide and its engineering geological significance," *Chinese Journal of Rock Mechanics and Engineering*, vol. 34, no. S1, pp. 3106–3115, 2015.

[26] J. J. Dong, C. C. Tsao, C. M. Yang, W. J. Wu, and R. Q. Huang, *The Geometric Characteristics and Initiation Mechanisms of the Earthquake-Triggered Daguangbao Landslide*, Springer Japan, 2017.

[27] S. H. Cui, *Microstructure and Static Dynamics Damage Mechanism of the Sliping Cataclastic Rock of the Largest Scale Landslide—A Case of Daguangbao Landslide in Anxian, [M.S. thesis]*, Chengdu University of Technology, Chengdu. (in Chinese), 2014.

[28] S. H. Cui, X. J. Pei, and R. Q. Huang, "Effects of geological and tectonic characteristics on the earthquake-triggered Daguangbao landslide, China," *Landslides*, vol. 15, pp. 649–667, 2018.

[29] R. Q. Huang, X. J. Pei, and T. B. Li, "Basic characteristic and formation mechanism of the largest scale landslide at Daguangbao occurred during the Wenchuan earthquake," *Journal of Engineering Geology*, vol. 16, no. 6, pp. 730–741, 2008.

[30] S. H. Cui, Q. W. Yang, X. J. Pei, R. Q. Huang, B. Guo, and W. F. Zhang, "Geological and morphological study of the Daguangbao landslide triggered by the Ms. 8.0 Wenchuan earthquake, China," *Geomorphology*, vol. 370, article 107394, 2020.

[31] S. H. Cui, X. J. Pei, Y. Jiang et al., "Liquefaction within a bedding fault: Understanding the initiation and movement of the Daguangbao landslide triggered by the 2008 Wenchuan earthquake (Ms = 8.0)," *Engineering Geology*, vol. 295, article 106455, 2021.

[32] R. Q. Huang, W. F. Zhang, and X. J. Pei, "Engineering geological study on Daguangbao landslide," *Journal of Engineering Geology*, vol. 22, no. 4, pp. 557–585, 2014.

[33] R. Q. Huang, X. J. Pei, X. M. Fan, W. F. Zhang, S. G. Li, and B. L. Li, "The characteristics and failure mechanism of the largest landslide triggered by the Wenchuan earthquake, May 12, 2008, China," *Landslides*, vol. 9, no. 1, pp. 131–142, 2012.

[34] R. Q. Huang, X. J. Pei, and S. H. Cui, "Cataclastic characteristic and formation mechanism of rock mass sliding zone of Daguangbao landslide," *Chinese Journal of Rock Mechanics and Engineering*, vol. 35, no. 1, pp. 1–15, 2016.

[35] China Geological Survey, CGS, *Regional Geological Map of Sichuan Province (1:50, 000)*, Geological Press, 1995.

[36] Z. J. Wu, D. Zhang, S. N. Wang, C. Liang, and D. Y. Zhao, "Dynamic-response characteristics and deformation evolution of loess slopes under seismic loads," *Engineering Geology*, vol. 267, article 105507, 2020.

[37] L. Q. Li, N. P. Ju, S. Zhang, and X. X. Deng, "Shaking table test to assess seismic response differences between steep bedding and toppling rock slopes," *Bulletin of Engineering Geology and the Environment*, vol. 78, no. 1, pp. 519–531, 2019.

[38] G. W. Liu, D. Q. Song, Z. Chen, and J. W. Yang, "Dynamic response characteristics and failure mechanism of coal slopes with weak intercalated layers under blasting loads," *Civil Engineering*, vol. 2020, article 5412795, pp. 1–18, 2020.

[39] P. Bettess and O. C. Zienkiewicz, "Diffraction and refraction of surface waves using finite and infinite elements," *International Journal for Numerical Methods in Engineering*, vol. 11, no. 8, pp. 1271–1290, 1977.

[40] D. Q. Song, X. L. Liu, J. Huang, E. L. Wang, and J. M. Zhang, "Characteristics of wave propagation through rock mass slopes with weak structural planes and their impacts on the seismic response characteristics of slopes: a case study in the middle reaches of jinsha river," *Bulletin of Engineering Geology and the Environment*, vol. 80, no. 2, pp. 1317–1334, 2021.

[41] S. A. Mousavi, M. Bastami, and S. M. Zahrai, "Large-scale seismic isolation through regulated liquefaction: a feasibility study," *Earthquake Engineering and Engineering Vibration*, vol. 15, no. 4, pp. 579–595, 2016.

[42] L. Zhu, X. J. Pei, S. H. Cui, S. Y. Wang, X. C. Zhang, and Y. F. Liang, "On the initiation mechanism of the Daguangbao landslide triggered by the 2008 Wenchuan (Ms 7.9) earthquake," *Soil Dynamics and Earthquake Engineering*, vol. 137, article 106272, 2020.

[43] Y. H. Hatzor, A. Zur, and Y. Mimran, "Microstructure effects on microcracking and brittle failure of dolomites," *Tectonophysics*, vol. 281, no. 3-4, pp. 141–161, 1997.

[44] J. T. Gomez, A. Shukla, and A. Sharma, "Static and dynamic behavior of concrete and granite in tension with damage," *Theoretical and Applied Fracture Mechanics*, vol. 36, no. 1, pp. 37–49, 2001.

[45] A. A. Griffith, "VI. The phenomena of rupture and flow in solids," *Philosophical Transactions of the Royal Society of London*, vol. 221, no. 582-593, pp. 163–198, 1921.

[46] X. J. Pei, S. H. Cui, and R. Q. Huang, "A model of initiation of Daguangbao landslide: dynamic dilation and water hammer in sliding zone during strong seismic shaking," *Chinese Journal of Rock Mechanics and Engineering*, vol. 37, no. 2, pp. 430–448, 2018.

[47] X. J. Li, Z. H. Zhou, H. Y. Yu et al., "Strong motion observations and recordings from the great Wenchuan earthquake," *Earthquake Engineering and Engineering Vibration*, vol. 7, no. 3, pp. 235–246, 2008.

[48] J. He, S. W. Qi, Y. S. Wang, and C. Saroglou, "Seismic response of the lengzhuguan slope caused by topographic and geological effects," *Engineering Geology*, vol. 265, article 105431, 2020.

[49] S. H. Cui, H. Wu, X. J. Pei, Q. W. Yang, R. Q. Huang, and B. Guo, "Characterizing the Spatial Distribution, Frequency, Geomorphological and Geological Controls on Landslides Triggered by the 1933 Mw 7.3 Diexi Earthquake," *Geomorphology*, vol. 403, article 108177, 2022.

[50] D. Q. Song, A. L. Che, R. J. Zhu, and X. R. Ge, "Natural frequency characteristics of rock masses containing a complex geological structure and their effects on the dynamic stability of slopes," *Rock Mechanics and Rock Engineering*, vol. 52, no. 11, pp. 4457–4473, 2019.